Research Square

Preprints are preliminary reports that have not undergone peer review.
They should not be considered conclusive, used to inform clinical practice,
or referenced by the media as validated information.

Multi-target design of hydroxyethylamine derivatives for Alzheimer's disease using 2D-QSAR, molecular docking, molecular dynamics simulations, and pharmacokinetic profiling against BACE1, AChE, D2 dopamine receptor, and FGFR3

Muhammad Abubakar Dagoli

muhammaddagoli@gmail.com

University of Abuja

Ahmed Umar

University of Abuja

Fabian Augu Ugbe

University of Abuja

Emmanuel Isreal Edache

University of Maiduguri

Research Article

Keywords: Alzheimer's disease, Hydroxyethylamine, Molecular docking, Molecular dynamics simulation

Posted Date: September 11th, 2026

DOI: https://doi.org/10.21203/rs.3.rs-10808443/v1

License: This work is licensed under a Creative Commons Attribution 4.0 International License.
Read Full License

Additional Declarations: No competing interests reported.

Title: Multi-target design of hydroxyethylamine derivatives for Alzheimer's disease using 2D-QSAR, molecular docking, molecular dynamics simulations, and pharmacokinetic profiling against BACE1, AChE, D2 dopamine receptor, and FGFR3.

Muhammad Abubakar Dagoli[a,b,*],
Ahmed Umar[a],
Fabian Audu Ugbe[a],
Emmanuel Israel Edache[c]

[a] *Department of Chemistry, University of Abuja, Gwagwalada, FCT Abuja, Nigeria.*
[b] *Chemical & Non-Petrochemical Industrial Development Department, Federal Ministry of Industry, Trade and Investment, Garki, Area 1, FCT Abuja, Nigeria.*
[c]Department *of Pure and Applied Chemistry, Faculty of Physical Sciences, University of Maiduguri, Maiduguri, Borno State, Nigeria.*

* Corresponding author.

E-mail addresses:
muhammaddagoli@gmail.com (M.A. Dagoli),
ahmed.umar@uniabuja.edu.ng (A. Umar),
ugbefabianaudu@gmail.com (F.A. Ugbe),
edacheson2004@gmail.com (E.I. Edache).

Abstract

Alzheimer's disease (AD) is a multifactorial neurodegenerative disorder that demands therapeutic strategies capable of modulating multiple pathological targets. In this study, we designed a focused set of 10 hydroxyethylamine-based compounds as multi-target directed ligands (MTDLs) aimed at four key Alzheimer's-related targets: BACE1, acetylcholinesterase (AChE), the D2 dopamine receptor, and FGFR3. To rank the most promising candidates, we applied an end-to-end in silico pipeline that integrated 2D QSAR modeling, molecular docking, 200 ns all-atom molecular dynamics (MD) simulations, endpoint binding free-energy estimates (using LIE, MM/PBSA, and MM/GBSA), and comprehensive pharmacokinetic profiling. The final 2D QSAR model showed solid statistical performance ($R^2 = 0.8545$, $Q^2LOO = 0.7965$, $F = 29.37$), satisfied standard criteria for predictivity, and passed Y-randomization checks; its applicability domain was further clarified through leverage analysis. Molecular docking revealed favorable binding modes and interactions of the designed compounds within the active sites of all four target proteins, with several derivatives exhibiting higher predicted affinities than the reference inhibitor and the template ligand 10. 200 ns MD simulations, principal component analysis (PCA), and binding free energy calculations confirmed the structural stability and thermodynamic favorability of the top protein-ligand complexes. Lead candidates of the designed analogs B2 and B5 demonstrated MM/GBSA binding free energy of -51.45kcal/mol and -50.64kcal/mol respectively. In silico pharmacokinetic and ADMET profiling showed that B2 and B5 possess high drug-likeness compliance (Lipinski's rule of five) and favourable blood-brain barrier permeability (Log BB = 0.129 for B2). Therefore, these findings highlight B2 and B5 as promising multi-target scaffolds for further experimental validation and optimization toward effective AD therapeutics.

Keywords:

Alzheimer's disease, Hydroxyethylamine, Molecular docking, Molecular dynamics simulation

1. Introduction

Alzheimer's disease (AD) is a progressive neurodegenerative disorder and the most common cause of dementia worldwide, characterized by memory loss, cognitive decline, and eventual loss of functional independence (Azmal *et al*., 2025; Hussain *et al.*, 2022; Hossain & Hussain, 2025). Despite decades of research, disease-modifying therapies remain limited, largely because AD is driven not by a single pathological event but by a complex network of interrelated mechanisms, including amyloid-β accumulation, cholinergic dysfunction, oxidative stress, neuroinflammation, and synaptic failure (Azmal *et al*., 2025; Chen *et al.*, 2022). This multifactorial nature has made the classical 'one drug, one target' strategy insufficient, thereby shifting attention toward multi-target-directed ligands (MTDLs) as a more realistic approach for AD intervention (Hossain & Hussain, 2025; Bajda *et al*., 2011). Modern therapeutic approaches have therefore shifted toward developing MTDLs that can influence multiple disease pathways simultaneously to address this complex etiology. (Ramsay *et al*., 2018).

Two of the most studied targets in AD are β-site amyloid precursor protein cleaving enzyme 1 (BACE1) and acetylcholinesterase (AChE). BACE1 sits at a key step in the amyloidogenic pathway; blocking it should reduce production of neurotoxic amyloid-β peptides. AChE inhibitors, by contrast, act on the cholinergic system: they prevent acetylcholine breakdown, thereby boosting cholinergic transmission and offering temporary symptomatic relief in memory and cognition (Gheidari et al., 2024; Bazzari & Bazzari, 2022; Peitzika & Pontiki, 2023). Beyond these, dopaminergic dysfunction has been linked to cognitive and behavioral symptoms in AD, making dopamine D2 receptors an attractive auxiliary target for ligands that could address both neurochemical imbalance and symptom modulation (Pasieka et al., 2021). More recently, fibroblast growth factor receptor 3 (FGFR3) has been shown to promote tau internalization after amyloid-β exposure, thereby accelerating tau pathology in AD (Bocharov et al., 2013; Kim et al., 2024). A ligand that can engage more than one of these targets may therefore provide a broader therapeutic profile than a single-target agent (Guerguer et al., 2025).

Hydroxyethylamine-based (HEA) scaffolds have long been of interest in medicinal chemistry. Their structural flexibility and track record in aspartyl protease inhibitor design make them attractive starting points (Neumann, 2011; Velcicky et al., 2019). In the context of AD, hydroxyethylamine derivatives have emerged as promising multi-functional candidates, with

reported activity against BACE1 and additional interactions relevant to symptom control or disease modification (Neumann, 2011). Their appeal goes beyond raw potency: the HEA core allows fine-tuning of physicochemical properties to improve central nervous system exposure, selectivity, and overall drug-likeness (Neumann, 2011). This balance matters in AD drug discovery, where compounds must not only be potent but also show suitable pharmacokinetics and blood–brain barrier compatibility to reach the brain at therapeutically relevant levels (Ugbe et al., 2022; Ugbe et al., 2024; Edache et al., 2025).

Computational methods have become central to modern drug design because they enable rapid triaging of compounds before synthesis and biological testing (Ugbe et al., 2023). QSAR modeling can highlight which structural features drive activity and thereby guide rational optimization, while molecular docking helps clarify how ligands recognize and bind within target active sites (Vinay et al., 2023; Ugbe et al., 2024). Molecular dynamics (MD) simulations add another layer by probing the stability of protein–ligand complexes over time, capturing dynamic behavior that static docking misses (Ugbe et al., 2022; Ugbe et al., 2023a; Edache et al., 2024). In parallel, ADMET and pharmacokinetic profiling are now routinely used to filter for compounds with acceptable absorption, distribution, metabolism, excretion, and toxicity early in the pipeline (Ugbe et al., 2024; Edache et al., 2024; Bozkır et al., 2026).

Against this backdrop, combining GA-MLR QSAR, multi-protein docking, MD simulation, and pharmacokinetic evaluation offers a practical framework for identifying promising anti-AD candidates. Genetic algorithm–multiple linear regression (GA-MLR) models are particularly useful for sifting through large descriptor spaces to find the most informative features and for building interpretable structure–activity relationships that support lead optimization (Ugbe et al., 2022; Ugbe et al., 2023a; Ugbe et al., 2023b; Edache et al., 2024). When paired with docking against BACE1, AChE, FGFR3, and dopamine D2 receptors, such models can help reveal whether hydroxyethylamine derivatives have the multi-target profile needed for AD therapy. This integrated workflow mirrors recent trends in multi-target AD drug discovery, where computational tools are increasingly used to narrow chemical space, improve efficiency, and strengthen the rationale for experimental follow-up (Jiansong et al., 2015; Ugbe et al., 2021; Vinay et al., 2023). In the present study, we therefore set out to design new multi-target-directed hydroxyethylamine derivatives for AD and to evaluate them using an integrated in silico strategy. Our workflow combines a 5-descriptor GA-MLR QSAR model with multi-protein molecular docking against BACE1, AChE, FGFR3, and dopamine D2 receptors, followed by MD simulation and ADMET/pharmacokinetic profiling. Through this polypharmacological approach, we rationally

design and validate novel multifunctional HEA candidates engineered to bind and inhibit BACE1, AChE, and FGFR3, while simultaneously modulating dopamine D2 receptors to achieve improved neuroprotective and neuropsychiatric profiles.

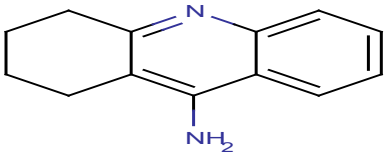
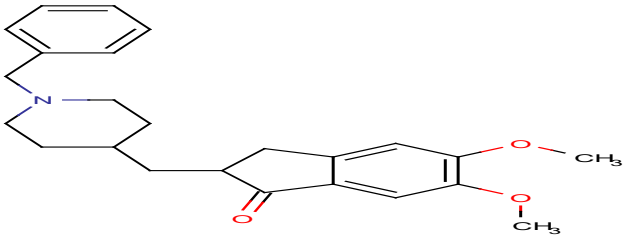
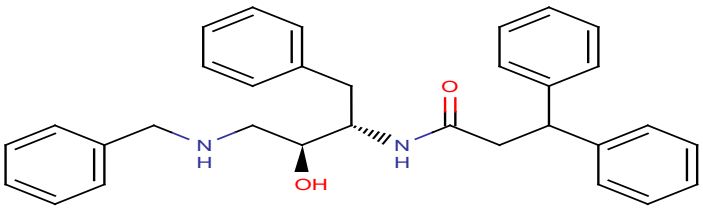
2. Materials and methods

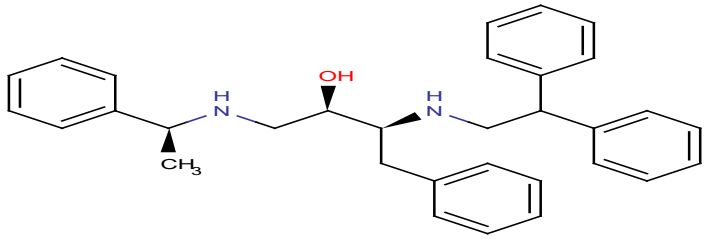
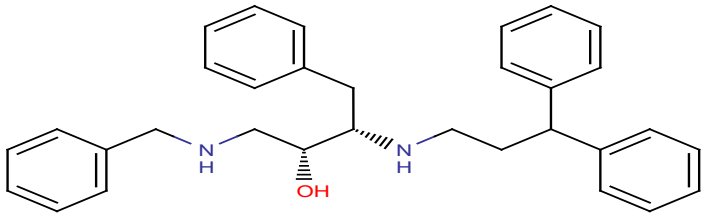
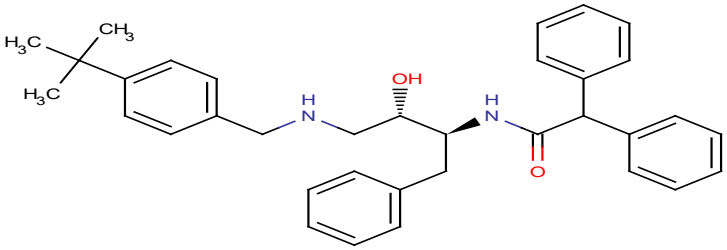
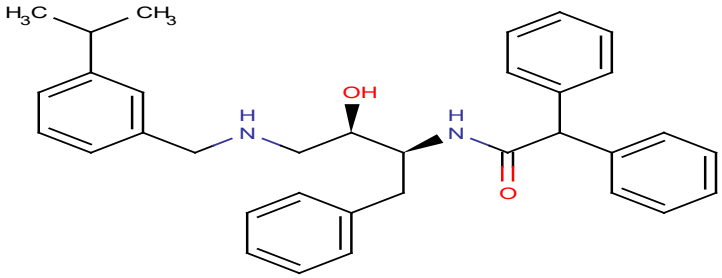
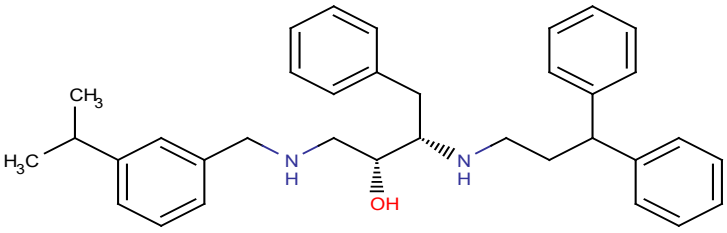
2.1. Selection of ligands for the study

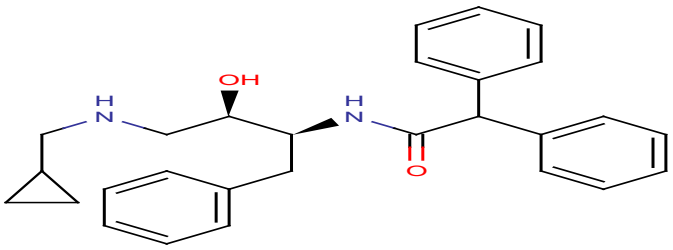
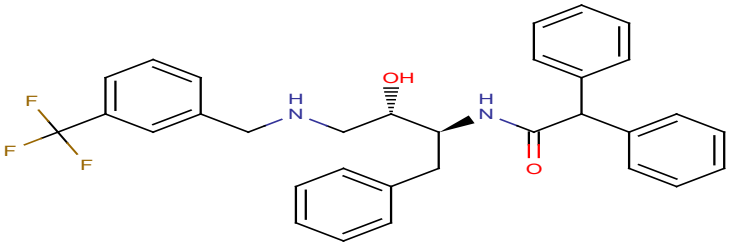
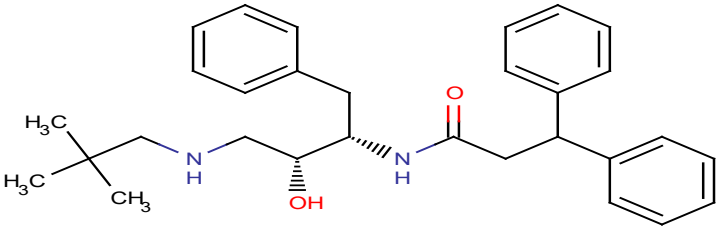
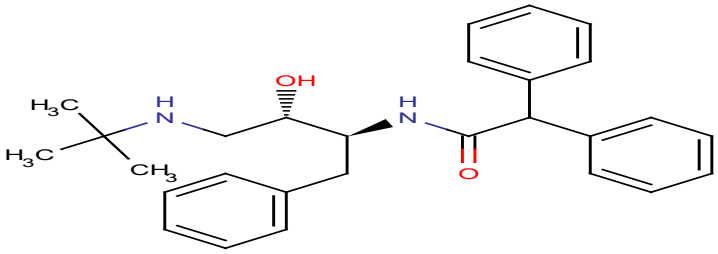
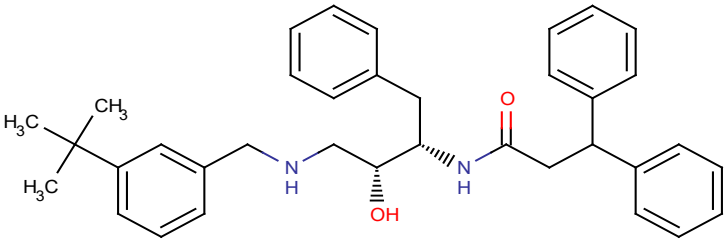
A set of thirty-nine (39) hydroxyethylamine derivatives (ligands) with inhibitory activity against disease-modifying targets, β-secretase enzyme (BACE1), butyrylcholinesterase (BuChE), and γ-aminobutyric acid transporters (GATs) was retrieved from the PubChem database (AID 1762427) reported by Pasieka *et al*., 2021. The values of minimum inhibitory concentration (IC_{50}) expressed in μM were transformed into pIC_{50} using the expression $-\log_{10}[IC_{50} \times 10^{-6}]$ to normalize potency data for computational modelling (QSAR) as shown in Table 1.

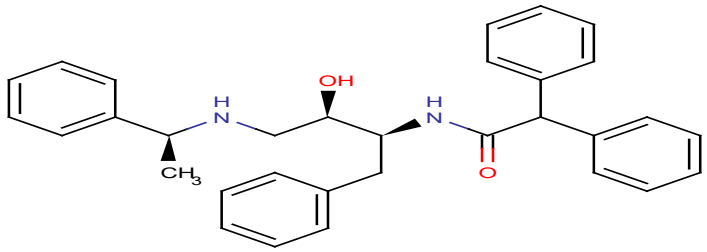
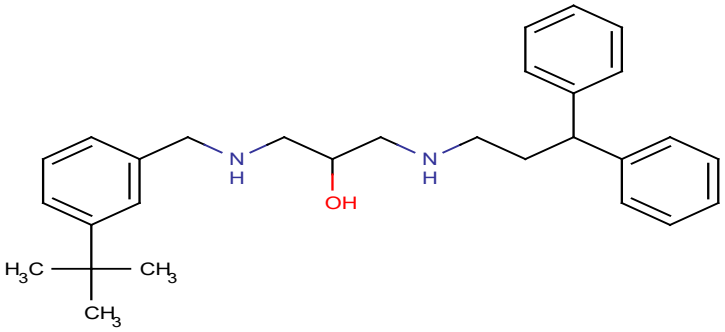
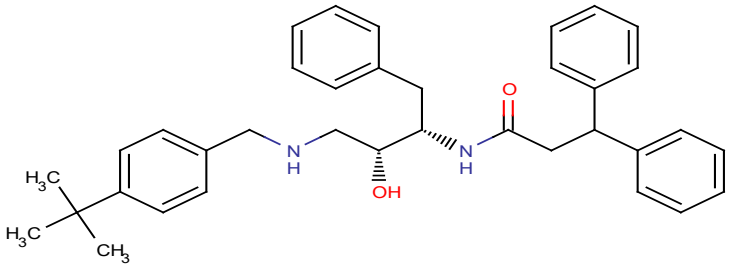
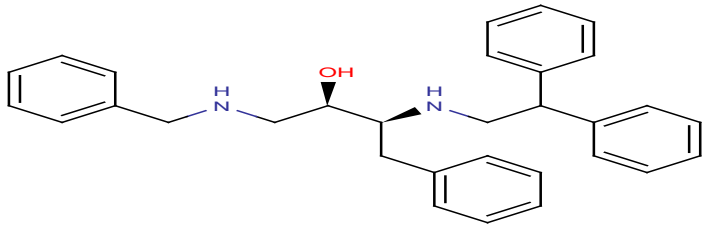
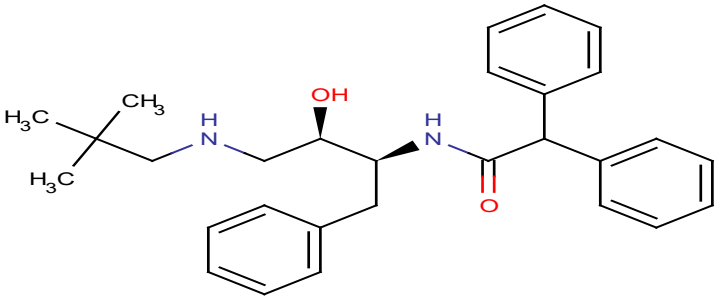
Table 1

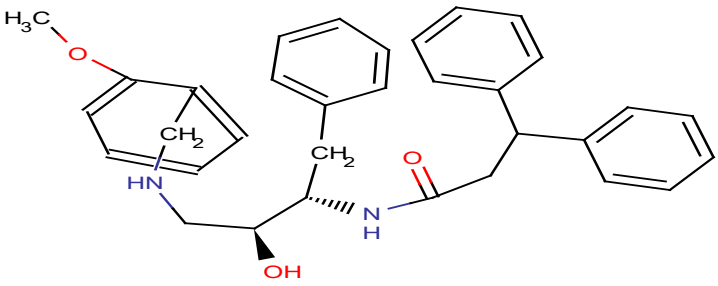
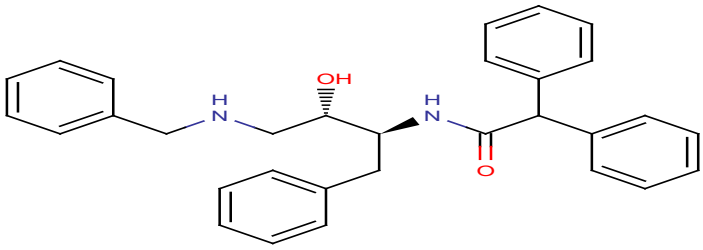
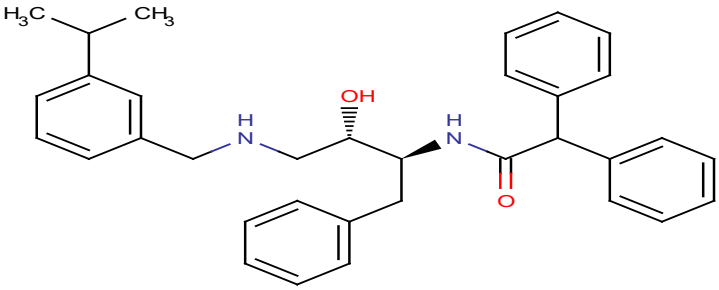
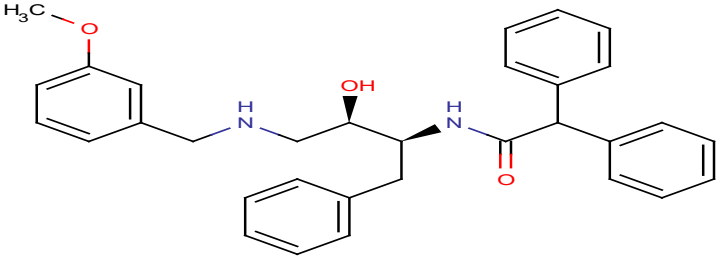
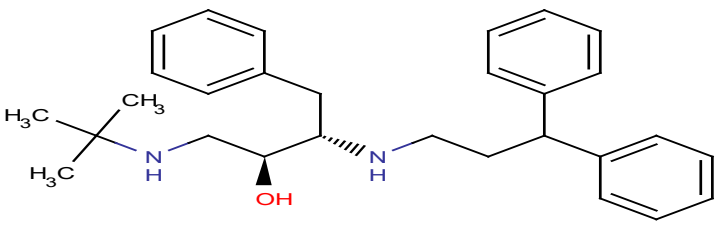
The molecular structures of hydroxyethylamine derivatives with PubChem compound identification (CID) number, half-maximal inhibitory concentration (IC_{50}), and their pIC50 values.

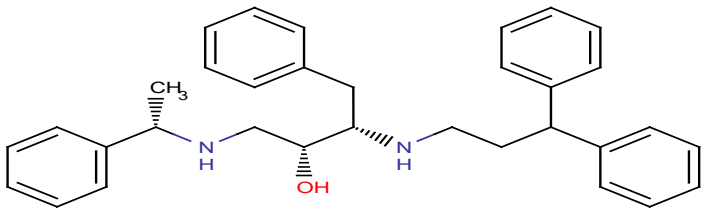
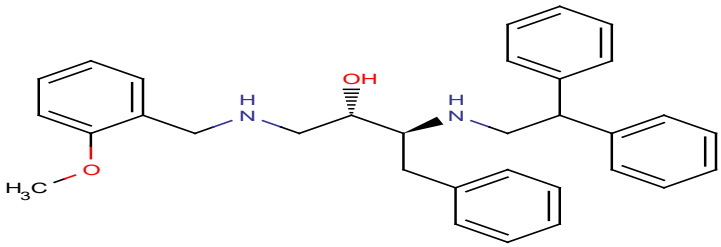
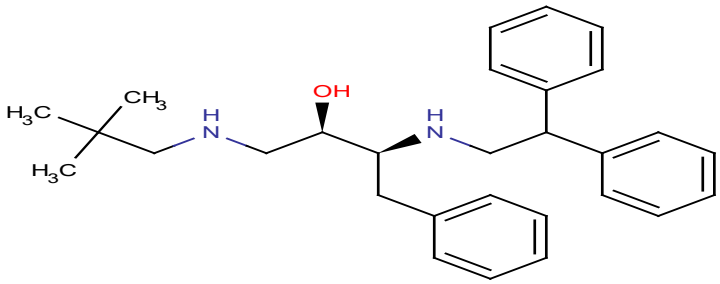
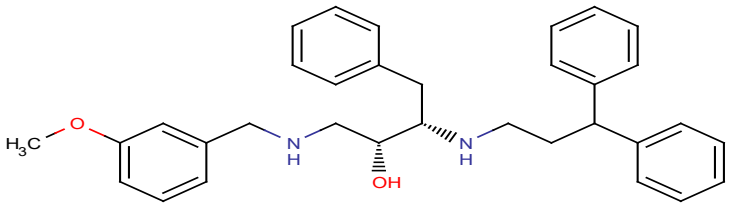
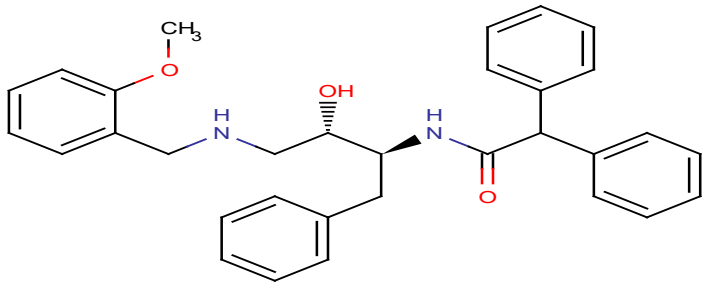
S/N	CID	Molecular Structure	IC_{50} (μM)	pIC_{50}
1	1935		0.015	7.8239
2	3152		1.83	5.7375
3	164609475		2.94	5.5317

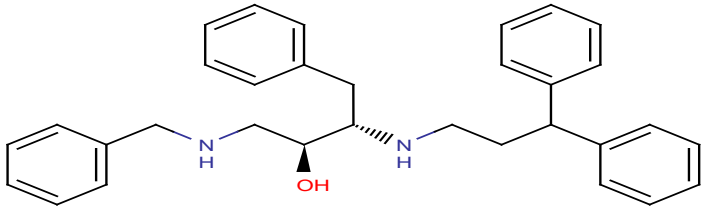
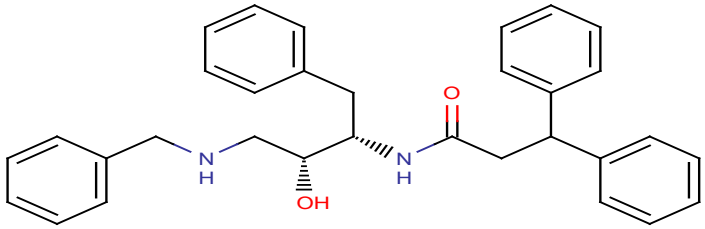
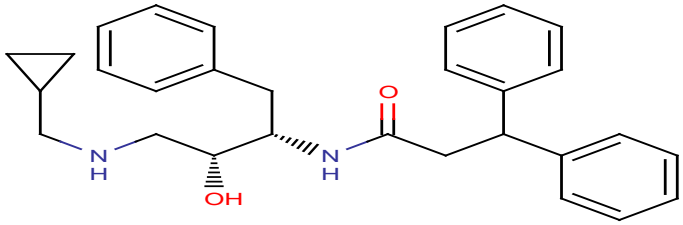
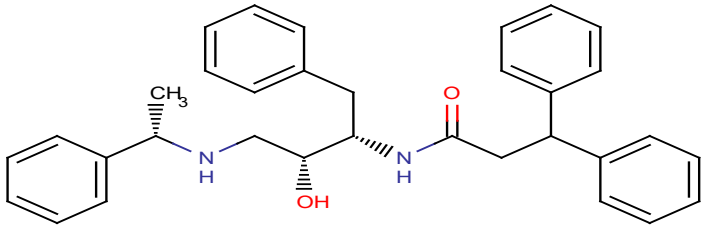
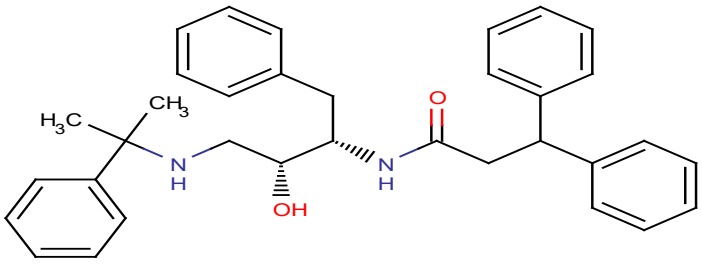
4	164609916		0.95	6.0223
5	164610030		1.54	5.8125
6	164610907		3.44	5.4634
7	164611185		0.5	6.301
8	164611490		1.84	5.7352

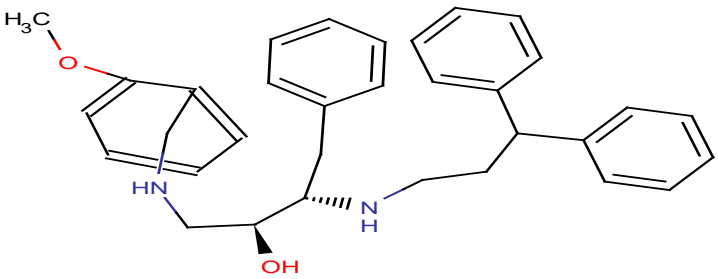
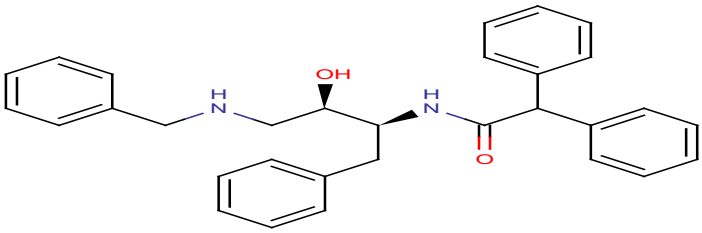
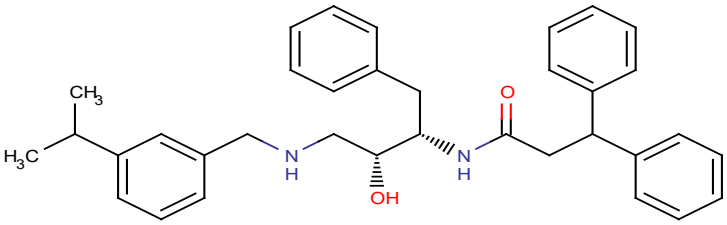
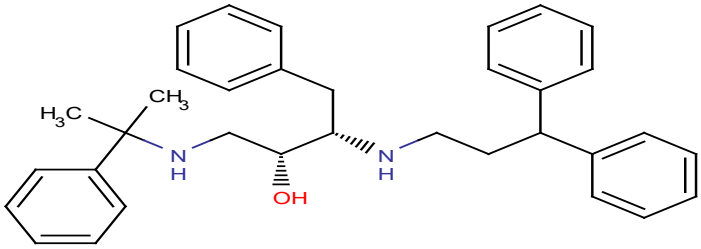
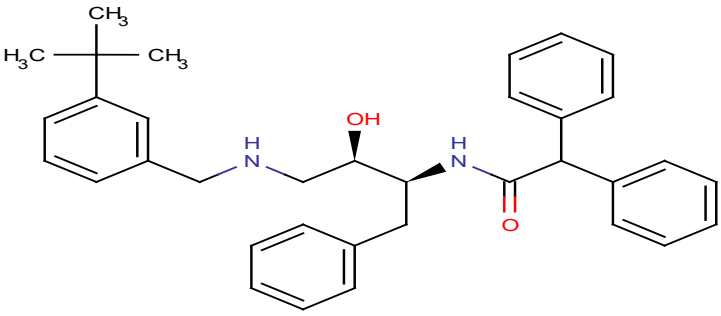
9	164612391		3.21	5.4935
10	164614126		0.39	6.4089
11	164614314		2.77	5.5575
12	164615874		0.84	6.0757
13	164615921		0.45	6.3468

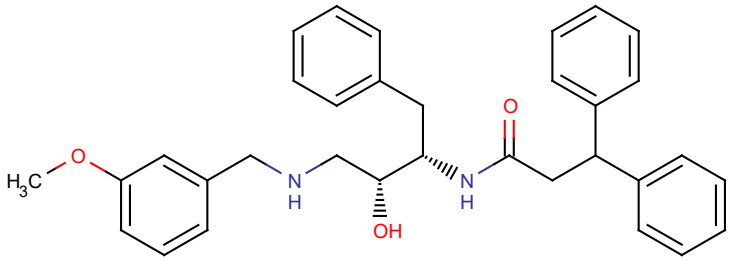
14	164616358		1.82	5.7399
15	154701599		2.92	5.5346
16	164617334		0.17	6.7696
17	164617454		0.95	6.0223
18	155920141		0.1	7

19	164617714		0.33	6.4815
20	164618064		0.23	6.6383
21	164620211		0.2	6.699
22	164620393		1.55	5.8097
23	164620627		0.19	6.7212

24	164621650		0.98	6.0088
25	164621802		0.32	6.4949
26	164622120		0.59	6.2291
27	164622565		2.04	5.6904
28	164623463		0.11	6.9586

29	164623763		0.65	6.1871
30	164623843		1.38	5.8601
31	164624990		3.23	5.4908
32	164625198		8.86	5.0526
33	164625351		3.23	5.4908

34	164626044		1.01	5.9957
35	164626646		1.51	5.821
36	164627701		0.65	6.1871
37	164627928		1.6	5.7959
38	164628439		0.06	7.2218

39	164628732		1.28	5.8928

2.2. Preparation of ligands for the study

The SMILES strings (Supplementary Table 1) were converted into 2D Spatial Data File (SDF) structures using MarvinSketch (Table 1), and subsequent energy minimization was performed using Avogadro software (Hanwell *et al*., 2012). Geometry optimization and energy minimization were performed using the Merck molecular force field (MMFF94). The optimized species were saved in the SDF format to facilitate the study of QSAR (Edache *et al*., 2024b). The primary aim of the QSAR approach is to derive interpretable relationships from numerical molecular descriptors, enabling the prediction of biological activity for new compounds. Practically, this involves converting descriptors computed with Pharmaceutical Data Exploration Laboratory (PaDEL-Descriptor) software v2.21 into a mathematical model that links those descriptors to the biological endpoint (pIC_{50}) (Yab, 2011; Edache *et al*., 2024b).

2.3. Building 2D-QSAR and modelling

For the model development, the optimized ligand structures and their computed molecular descriptors (PaDEL-Descriptor v2.21) were assembled into an n × m data matrix and used as input for QSAR modeling. The dataset was partitioned into training and external test sets to allow independent model building and validation. Approximately 80% of the compounds were assigned to the training set and the remaining 20% to the test set such that points representing test compounds are located within the descriptor space spanned by the training set (Arthur *et al*., 2018). Multiple linear regression (MLR) was employed to construct the 2D-QSAR models, relating the dependent variable (pIC_{50}) to selected molecular descriptors. Descriptor reduction and multicollinearity control were achieved using the genetic function approximation–multiple linear regression (GA-MLR) procedure implemented in QSARIN v2.2.4, after descriptor calculation with PaDEL. MLR models were fit by the ordinary least squares method, producing regression equations of the form:

$$Y = b_1x_1 + b_2x_2 + b_3x_3 \ldots + c, \qquad (1)$$

where Y is pIC_{50}, b_1 are regression coefficients, x_1 are descriptor values, and c is the intercept. (Gramatica *et al*., 2013; Edache *et al*., 2024b; Arthur *et al*., 2022). Furthermore, the relative contribution of each descriptor in the built QSAR model is shown by the mean effect (ME) values, defined as (Eq. 2):

$$MF = \frac{\beta_j \sum_{i=1}^{n} D_{ij}}{\sum_{j=1}^{m} \beta_j \sum_{i=1}^{n} D_{ij}} \quad (2)$$

where *βj* represents the coefficient *j* descriptor in the model, *Dj* equals each descriptor's value for each molecule in the training set, *m* represents the number of descriptors present in the model, and *n* is the total number of compounds in the training set (Adeniji *et al*, 2019). The variance inflation factor (VIF), defined as (Eq. 3), shows the extent of inter-correlation between the descriptors.

$$VIF = \frac{1}{1-R^2} \quad (3)$$

R^2 represents the coefficient of correlation of the multiple regression between the variables in the model. VIF equal to 1 shows that no inter-correlation exists for each variable, and for VIF values within the range of 1–5, the related model is acceptable, and where VIF is above 10, the related model is unstable and therefore cannot be accepted (Abdullahi *et al*., 2019).

2.4. Outlier detection and data cleaning

For finalizing the chemometric models, we performed a comprehensive outlier diagnostic workflow to preserve the structural integrity and generalizability of the training set (Todeschini & Consonni, 2009). During initial GA-MLR exploratory cycles, two compounds, Compound 16 (pIC_{50} = 6.7696) and Compound 18 (pIC_{50} = 7.0000), consistently displayed extreme anomalies. These molecules produced large, unsystematic standardized residuals (exceeding three times the mean absolute error) regardless of assignment to the training or validation sets, thereby perturbing the local regression plane and behaving as activity cliffs. In line with established QSAR practice, these compounds were therefore classified as structural/biological outliers, likely reflecting unique electronic or steric interactions that do not conform to the linear SAR pattern of the series. To prevent artificial distortion of the multidimensional calibration space, Compounds 16 and 18 were excluded from the final modeling. This cleaning step reduced the dataset from 39 to 37 compounds, yielding a robust training set of 25 compounds and an external test set of 6 compounds.

2.5. Model quality assessment and validation

The model performance and statistical robustness were assessed by standard metrics such as the number of compounds in regression (n), number of variables (descriptors) (K), degrees of freedom (DF), R^2 (the squared correlation coefficient), F-test, cross-validated R^2 (Q^2, e.g., $_{LOO\text{-}CV}$), external predictive R^2 (R^2_{pred}), and standard errors. Randomization statistics (rand R^2, rand Q^2) and

the significance parameter α from Y-randomization were also evaluated. Models were considered acceptable when $R^2 > 0.6$, $Q^2 > 0.6$, and $R^2_{pred} > 0.5$ (Gramatica, 2007), consistent with commonly used thresholds. Low standard errors for R^2, Q^2, and R^2_{pred} were used to judge absolute fit and predictive precision (Gramatica *et al*., 2013; Papa *et al*., 2007).

2.6. Y-scrambling test

To verify that model performance was not due to chance correlation, Y-scrambling (Y-randomization) was performed on the training set. The activity values were randomly permuted while descriptors remained unchanged, and MLR models were rebuilt. The scrambled models are expected to exhibit substantially lower R^2 and Q^2 values; in this study, 100 Y-randomization runs were performed (Edache *et al*., 2015).

2.7. Applicability domain

The applicability domain analysis was employed to determine if the designed compounds fall within the chemical space of the predictive model. Williams plots were utilized to visualize the relationship between standardized residuals and leverage (*h*), identifying any structural outliers that exceed the warning leverage (*h**) (Edache *et al*., 2015; Edache *et al*., 2025; Ugbe *et al*., 2022a, Ugbe *et al*., 2022b).

2.8. Target protein setup and docking procedure

The three-dimensional (3D) structure of the enzymes BACE1 (PDB ID: 2ZHV), AChE (PDB ID: 4EY7), D2 dopamine receptor (PDB ID: 6CM4), and FGFR3 (PDB ID: 6LVM) were retrieved from the Protein Database (PDB) (http://www. rcsb.org). Each receptor was prepared by deleting heteroatoms and crystallographic water molecules. Thereafter, the proteins were prepared and minimized using the MzDock software (Kabier *et al*., 2024). The reliability of the docking protocol was corroborated by re-docking (Edache *et al*., 2025). At first, the native ligands were withdrawn from the protein binding site cavity, and the binding site was defined by applying the study ligands (Table 1) selection to obtain the ligand attributes as: centre x = 62.401, y = 46.016, z = 0.826, and size x = 60.75 Å, y = 75.75 Å, z = 57.75 Å for 2ZHV; centre x = -13.988, y = -43.905, z = 27.108, and size x = 34 Å, y = 14 Å, z = 26 Å for 4EY7; centre x = 9.177, y = 5.471, z = -8.665 and size x = 18 Å, y = 24 Å, z = 38 Å for 6CM4; centre x = -3.650, y = 0.227, z = 9.933, and size x = 36 Å, y = 44 Å, z = 32 Å for 6LVM. Docking of the prepared ligands together with reference drugs (donepezil, galantamine, rivastigmine) was performed using EasyDockVina v1.2.5. (Eberhardt *et al*., 2021). The pose with the lowest binding energy was chosen as the preferred docked model, and the final selection of the best pose was supported by analysis of conventional hydrogen bonds and other key noncovalent interactions. Lower binding energy

corresponds to a stronger predicted affinity. Re-docking produced an RMSD < 2 Å between the native crystal ligand and the best docked pose, confirming the protocol's validity. Docking results were visualized using Discovery Studio Visualizer.

2.9. ADMET and pharmacokinetic evaluation

The pharmacokinetic and toxicity profiles of the novel derivatives were conducted using SwissADME and pkCSM web servers to determine the candidates' suitability for subsequent *in vitro* and *in vivo* investigations (Edache *et al*., 2025; Daina *et al*., 2017; Ugbe *et al*., 2023a). The ADMET analyses are screened according to Lipinski's Rule of Five (Lipinski, 2002). The total polar surface area (TPSA), water partition coefficient (MlogP), number of rotatable bonds (Rot-bond), number of hydrogen bond donors (H-bond donor), number of hydrogen bond acceptors (H-bond acceptor), molecular weight (MW), and synthetic accessibility (SA) were computed.

2.10. Molecular dynamics simulation protocol

To characterize the conformational behavior and binding stability of the Alzheimer's protein–ligand complexes at atomic resolution, MD simulations were performed starting from the docked complexes and the 6CM4 crystal coordinates. Simulations were run with NAMD at 310 K (Edache *et al*., 2025; Ugbe *et al.*, 2024) for 200 ns. Simulation input files and ligand parameters were generated using the CHARMM-GUI website (http://www.charmm-gui.org/). Each system was energy-minimized and then equilibrated in two stages (NVT followed by NPT) at physiological temperature, with explicit solvation provided by the TIP3P water model (Edache *et al*., 2025). Trajectory analyses were carried out with VMD scripts to monitor stability and dynamics via Root-Mean-Square Deviation (RMSD), radius of gyration (RoG), and other relevant parameters, under periodic boundary conditions.

2.11. Free energy calculations: MM/GB(PB)SA and LIE

The binding free energy (ΔG_{bind}) of each protein–ligand complex was estimated using the Molecular Mechanics/Poisson-Boltzmann (General-Born) Surface Area MM-PB(GB)SA endpoint approach, which offers a practical compromise between computational cost and predictive accuracy (Edache *et al*., 2024). The calculated ΔG_{bind} combines the gas-phase molecular mechanics energy (ΔG_{MM}), the solvation free energy (ΔG_{sol}), and the conformational entropy term ($-T\Delta S$), as expressed in the following equations (Edache *et al*., 2025).

$$\Delta G_{bind} = G_{complex} - (G_{protein} + G_{ligand}) \quad (4)$$

$$\Delta G_{bind} = \Delta E_{gas} + \Delta G_{sol} - - T\Delta S \quad (5)$$

$$\Delta E_{gas} = \Delta E_{int} + \Delta E_{ELE} + \Delta E_{VDW} \quad (6)$$

$$\Delta G_{sol} = \Delta G_{polar} + \Delta G_{nonpolar} = \Delta G\text{GB} + \Delta G\text{SA} \quad (7)$$

$T\Delta S = T(\Delta S_{trans} + \Delta S_{rot} + \Delta S_{vib}$ (8)

Where ΔG_{bind} refers to the total binding free energy of the complex in kcal/mol, which is a combination of molecular mechanics gas phase energy (ΔE_{gas}), and solvation free energy (ΔG_{sol}) as displayed in equation 6. To quantify interaction energies between the hydroxyethylamine derivatives and active-site residues of 6CM4, MM-PB(GB)SA calculations were performed using CaFE and MOLAlCAL tools (Liu & Hou, 2016; Bai *et al*., 2021). MM-PB(GB)SA calculations employed a grid spacing of 1.0 Å, with internal and external dielectric constants set to 1.0 and 80.0, respectively. ΔG_{bind} values were computed from 100 representative snapshots sampled from equilibrated portions of the MD trajectories. In addition to MM-PB(GB)SA, the Linear Interaction Energy (LIE) method was applied as an independent end-state approach. For LIE analysis, each ligand was also simulated in the unbound state in explicit solvent under the same simulation conditions used for the protein–ligand complexes. The LIE coefficients for α, β, and γ were set to their default values of 0.18, 0.33, and 0.0, respectively. The binding free energy via the LIE approach is expressed as follows:

$LIE = \alpha(\Delta G_{LJ,\ bound-unbound}) + \beta(\Delta G_{LJ,\ bound-unbound}) + \gamma$ (9)

$\Delta G_{bind} = \alpha([V_{LJ,\ Lig-Surr}]_{bound} - [V_{LJ,\ Lig-Surr}]_{unbound}) + \beta([V_{Coul,Lig-Surr}]_{bound} - [V_{Coul,\ Lig-Surr}]_{unbound}) + \gamma$ (10)

The $[V_{LJ,\ Lig-Surr}]_{bound}$ and $[V_{LJ,\ Lig-Surr}]_{unbound}$ are the average Lennard-Jones (LJ) = van der Waals (vdw) interaction energies of two complex bound and unbound statuses. The $[V_{Coul,\ Lig-Surr}]_{bound}$ and $[V_{Coul,\ Lig-Surr}]_{unbound}$ are the average Coulombic (Coul) = electrostatic (ele) interaction energies from two protein-ligand bound or unbound status (Edache *et al*., 2025; Ugbe *et al*., 2023a).

3. Results and discussion

3.1. QSAR model evaluation and SAR discussion

Cheminformatics modelling of thirty-nine (39) hydroxyethylamine derivatives was performed to establish a quantitative relationship between their chemical structure and inhibitory activity. Using a Genetic Algorithm-Multiple Linear Regression (GA-MLR) procedure, a five-descriptor QSAR model was developed. The resulting model is expressed as:

pIC_{50} = 6.5890 - 0.0015 (**ATSC8m**) + 4.1467 (**AATSC7i**) + 16.6420 (**MATS4c**) - 0.6902 (**GATS5s**) + 0.7351 (**GATS6s**) Model 1 (11)

where **ATSC8m** is a centered 2D autocorrelation descriptor at topological lag 8, weighted by atomic mass. **AATSC7i** is an averaged centered 2D autocorrelation descriptor at lag 7, weighted by atomic ionization potential. **MATS4c** is a Moran 2D autocorrelation descriptor at lag 4, weighted by atomic charge. **GATS5s** is a Geary 2D autocorrelation descriptor at lag 5, weighted

by the atomic intrinsic state index. **GATS6s** is a Geary 2D autocorrelation descriptor at lag 6, also weighted by the atomic intrinsic state index.

(Fitting criteria)

R^2: 0.8545; R^2_{adj}: 0.8254; R^2-R^2_{adj}: 0.0291; LOF: 0.1060; Kxx: 0.3615; Delta K: 0.0130; $RMSE_{tr}$: 0.2205; MAE_{tr}: 0.1707; RSS_{tr}: 1.5073; CCC_{tr}: 0.9216; s: 0.2455; *F*: 29.3675.

(Internal validation criteria)

Q^2_{loo}: 0.7965; R^2-Q^2_{loo}: 0.0580; $RMSE_{cv}$: 0.2608; MAE_{cv}: 0.2043; $PRESS_{cv}$: 2.1084; CCC_{cv}: 0.8900; Q^2_{LMO}: 0.7681; R^2_{Yscr}: 0.1656; Q^2_{Yscr}: -0.3222; RMSE AV $_{Yscr}$: 0.5272.

(External validation criteria)

RMSE $_{ext}$: 0.3169; MAE $_{ext}$: 0.2529; PRESS $_{ext}$: 0.6025; R^2_{ext}: 0.1236; Q^2-F_1: 0.1620; Q^2-F_2: 0.0212; Q^2-F_3: 0.6995; CCC $_{ext}$: 0.3116; r2m aver.: 0.0297; r2m delta: 0.1204.

Predictions by LOO:

Exp(x) vs. Pred(y): R^2: 0.7974; R'2o: 0.7612; k': 0.9980; Clos': 0.0453; r'2m: 0.6458.

Pred(x) vs. Exp(y): R^2: 0.7974; R2o: 0.7965; k: 1.0001; Clos: 0.0011; r2m: 0.7738.

External predictions by the model equation:

Exp(x) vs. Pred(y): R^2: 0.1236; R'2o: -1.4315; k': 1.0062; Clos': 12.5786; r'2m: -0.0305.

Pred(x) vs. Exp(y): R^2: 0.1236; R2o: 0.0491; k: 0.9911; Clos: 0.6030; r2m: 0.0899.

The model exhibited good calibration statistics (R^2 = 0.8545, R^2_{adj} = 0.8254, $RMSE_{tr}$ = 0.2205, MAE_{tr} = 0.1707, *F* = 29.37), indicating an adequate fit to the training data. Internal validation confirmed its robustness, with Q^2_{LOO} = 0.7965, low $RMSE_{cv}$ (0.2608) and MAE_{cv} (0.2043), and satisfactory Y-scrambling results (R^2_{Yscr} = 0.1656, Q^2_{Yscr} = − 0.3222), which exclude chance correlations. The concordance correlation coefficients for training (CCC_{tr} = 0.9216) and cross-validation (CCC_{cv} = 0.8900), together with acceptable LOO prediction metrics (e.g., r2m and r′2m), further support the model's internal reliability. For the external test set, the model produced low prediction errors (MAE_{ext} = 0.2529, $RMSE_{ext}$ = 0.3169), indicating that the absolute deviations between experimental and predicted pIC_{50} values are small. Although the conventional external determination coefficient was low (R^2_{ext} = 0.1236), this behavior is attributable to variance compression arising from the narrow and clustered experimental pIC_{50} range in the test set, which mathematically deflates R^2_{ext} under such conditions. In this context, the Consonni–Todeschini Q^2F_3 metric provides a more reliable measure of external predictivity, and the value obtained (Q^2F_3 = 0.6995) demonstrates strong external performance, comfortably exceeding the commonly accepted threshold of 0.50 for quality QSAR models (Todeschini & Consonni, 2009; Todeschini et al., 2016; Gramatica, 2014; Chirico & Todeschini, 2017). In addition, the calculated descriptor

values, experimental and predicted activities (pIC_{50}), and corresponding residuals are listed in Table 2.

Table 2

Calculated descriptors, experimental and predicted pIC50 values, and residuals for the hydroxyethylamine derivatives

Ligand ID	ATSC8m	AATSC7i	MATS4c	GATS5s	GATS6s	pIC_{50}	Pred. pIC_{50}	Residuals
1	211.5546	-0.0763	0.1426	1.7286	0.9483	7.8239	7.8199	-0.0040
2	-337.9455	-0.0109	-0.0615	1.0066	1.2361	5.7375	5.6745	-0.0630
3	-579.1338	0.0082	-0.1188	1.2376	1.7788	5.5317	5.6884	0.1567
4	-405.1601	-0.0241	-0.0347	1.1394	1.5097	6.0223	6.1181	0.0958
5*	-392.4336	0.0081	-0.0522	1.1860	1.2594	5.8125	5.7395	-0.0730
6	-951.2766	-0.1972	-0.0396	1.6026	1.6364	5.4634	5.4807	0.0173
7	-452.3939	0.0526	-0.0419	1.6152	1.6214	6.3010	6.5346	0.2336
8*	-462.6133	0.1176	-0.0598	1.1519	1.2569	5.7352	5.7352	0.2489
9*	-83.1607	-0.0562	-0.0430	1.7061	1.7220	5.4935	6.1547	0.6612
10	-185.4853	-0.0979	-0.0334	0.9823	1.0735	6.4089	6.4122	0.0033
11	-1198.1895	0.0061	-0.1252	1.2447	1.7533	5.5575	5.6428	0.0853
12	-1073.1478	0.0563	-0.0158	1.5764	2.1000	6.0757	6.0965	0.0208
13	-1139.0154	0.1806	-0.1143	1.1689	1.7253	6.3468	6.4160	0.0692
14	-377.4329	-0.0296	-0.0416	1.5752	1.7668	5.7399	5.8896	0.1497
15	-835.2303	0.1305	-0.0705	1.0435	0.9617	5.5346	5.6466	0.1120
16^{E}	-1139.0154	-0.1193	-0.1147	1.1885	1.7514	6.7696		
17	-418.5456	-0.0742	-0.0266	1.2348	1.2460	6.0223	6.0080	-0.0143
18^{E}	-1004.8481	-0.0644	-0.0486	1.7150	1.6390	7.0000		
19*	-480.2221	0.0092	-0.0624	1.1874	1.6718	6.4815	6.3457	-0.1358
20	-389.4978	-0.0832	-0.0348	1.7053	1.6660	6.6383	6.1939	-0.4444
21	-452.3939	0.0526	-0.0419	1.6152	1.6214	6.6990	6.5346	-0.1644
22	-461.9458	-0.0056	-0.0442	1.6237	1.5902	5.8097	6.2097	0.4000
23	-1070.8686	0.1179	-0.0306	1.0261	2.0426	6.7212	6.6348	-0.0864
24*	-379.5535	0.0496	-0.0598	1.0982	1.5177	6.0088	5.8200	-0.1888
25	-306.1217	-0.0653	0.0207	1.1704	1.1841	6.4949	6.5828	0.0879
26	-1034.6144	-0.0591	-0.0436	1.2438	1.2600	6.2291	5.9650	-0.2641
27	-438.6129	0.0692	-0.0595	1.1300	1.1777	5.6904	5.6884	-0.0020
28	-296.9999	-0.0726	0.0092	1.6082	1.5670	6.9586	6.7218	-0.2368
29	-392.4336	0.0081	-0.0522	1.1860	1.2594	6.1871	5.7395	-0.4476
30	-579.1338	0.0082	-0.1188	1.2376	1.7788	5.8601	5.6884	-0.1717
31	-283.6063	0.0269	-0.1313	1.2310	1.8365	5.4908	5.5465	0.0557
32	-567.2741	0.0531	-0.1239	1.1500	1.8753	5.0526	5.3441	0.2915
33	-925.7956	0.0914	-0.1212	1.0777	1.9672	5.4908	5.0995	-0.3913
34	-273.6669	0.0080	-0.0009	1.1289	1.1965	5.9957	6.3347	0.3390
35	-389.4978	-0.0832	-0.0348	1.7053	1.6660	5.8210	6.1939	0.3729
36*	-644.9141	0.1260	-0.1221	1.1880	1.7347	6.1871	5.9775	-0.2096
37	-719.3243	0.0854	-0.0615	1.0248	1.7517	5.7959	5.9512	0.1553
38	-951.2766	0.1127	-0.0392	1.5824	1.6124	7.2218	6.9231	-0.2987
39	-645.1681	0.0747	-0.1156	1.1956	1.6965	5.8928	5.8355	-0.0573

* = test set ^{E} = excluded

As indicated in Table 2, the application of the genetic algorithm in combination with multiple linear regression (GA-MLR) yielded a QSAR model based on five descriptors that meets the commonly accepted criteria for a reliable QSAR model. The small residuals between experimental and predicted activities for both training and test sets (Table 2) indicate good predictive performance. The variance inflation factor (VIF) values of the five selected descriptors ranged from 1.5820 to 4.5751 (Table 3), well below the standard threshold of 5.0, indicating the absence of severe multicollinearity and confirming that the QSAR model is statistically stable. The statistical relevance of each descriptor was verified using an absolute t-statistic and two-tailed *p*-values. All five descriptors exhibited absolute t-Stat greater than 2.0, consistent with statistical significance of its contribution to the model (Adeniji *et al*., 2018; Ugbe *et al*., 2022b).

Table 3

Inter-correlation matrix and statistical parameters of the descriptors

Descriptor	ATSC8m	AATSC7i	MATS4c	GATS5s	GATS6s	VIF	ME	t-Stat	*p*-value
ATSC8m	1					2.4773	-0.0001	-6.15	1.3E-6
AATSC7i	0.2970	1				1.5820	0.1671	5.86	3.0E-6
MATS4c	0.3515	-0.3893	1			4.5751	0.8358	9.29	6.0E-10
GATS5s	-0.2902	-0.4005	0.4254	1		2.9451	-0.0358	-2.26	3.2E-2
GATS6s	-0.0908	0.2038	-0.5016	0.1814	1	2.3854	0.0330	3.16	3.9E-3

In addition, the p-values for all descriptors were below 0.05 at the 95% confidence level (Table 3), supporting the alternative hypothesis that there is a significant relationship between the descriptors in the model equation and the compounds' inhibitory activities. The mean effect (ME) values were used to assess the strength and direction of each descriptor's contribution to the inhibitory activity (Table 3). The magnitude of ME reflects the extent of influence, whereas its sign indicates whether the effect is positive or negative. MATS4c, AATSC7i, and GATS6s showed the largest positive ME values (0.8358, 0.1671, and 0.0330, respectively), suggesting that increasing these descriptor values is associated with higher inhibitory activity. By contrast, ATSC8m and GATS5s exhibited negative ME values (−0.0001 and −0.0358), indicating that an increase in these descriptors tends to decrease the inhibitory activity.

The agreement between experimental and predicted pIC50 values for the training and test sets is shown in Figure 1. The close clustering of data points around the ideal regression line (y = x) indicates good predictive performance and a strong fit of the model. Residual analysis (Figure 2) shows a random distribution of standardized residuals around zero within the accepted limits, suggesting the absence of systematic error and heteroscedasticity.

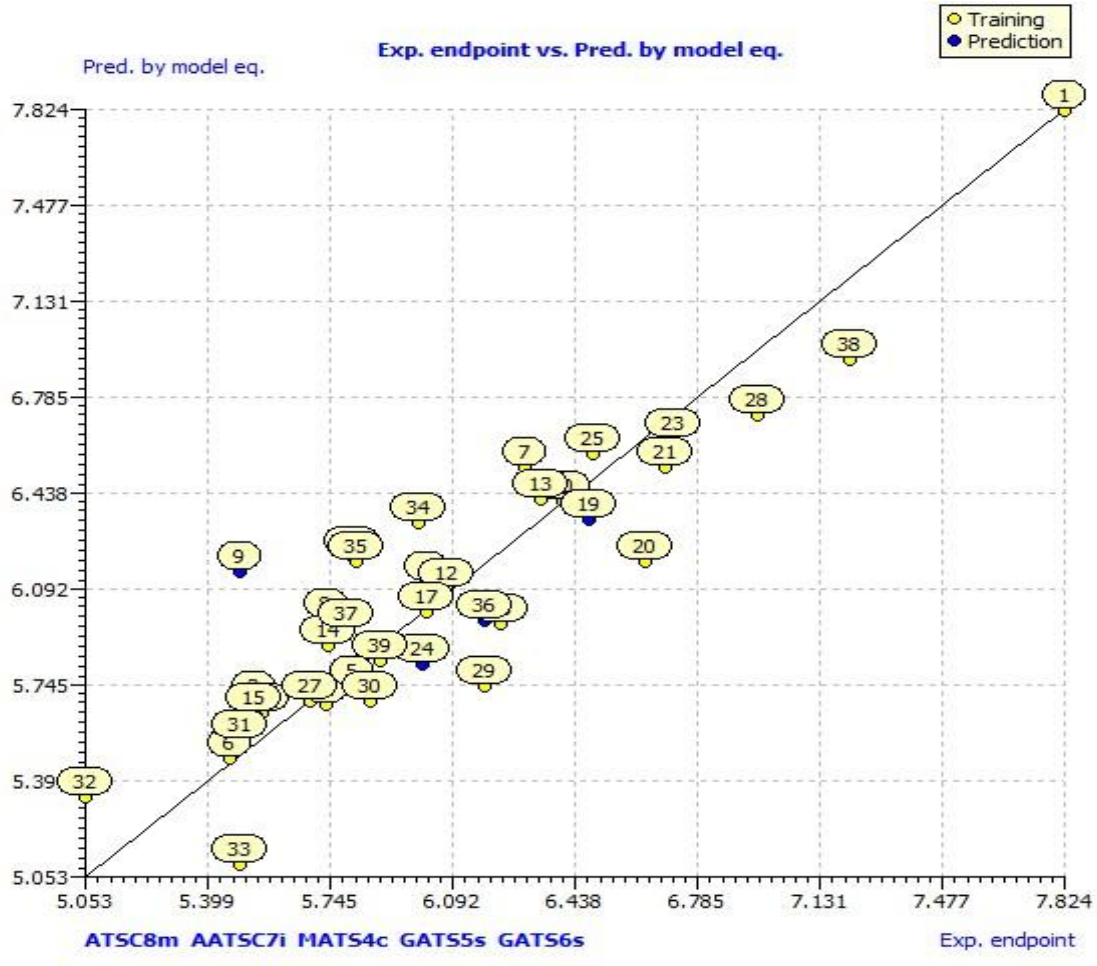


Figure 1. Experimental versus predicted pIC_{50} values for the hydroxyethylamine derivatives using the GA-MLR QSAR model

Applicability domain analysis was performed using the Williams plot of standardized residuals versus leverage values (Figure 3). All dataset compounds fell strictly within the standardized residual bounds of ± 3.0 standard deviations, confirming the complete absence of response outliers. Although Compound 9 displayed the highest positive standardized residual (≈ +2.88), it remained safely within the statistical boundary. Regarding structural space, no compound exceeded the warning leverage (h^* = 0.581). Compounds 1 and 23 recorded the highest leverages (h = 0.480), positioning them as structurally influential molecules that define the outer boundary of the chemical space while remaining valid within the domain.

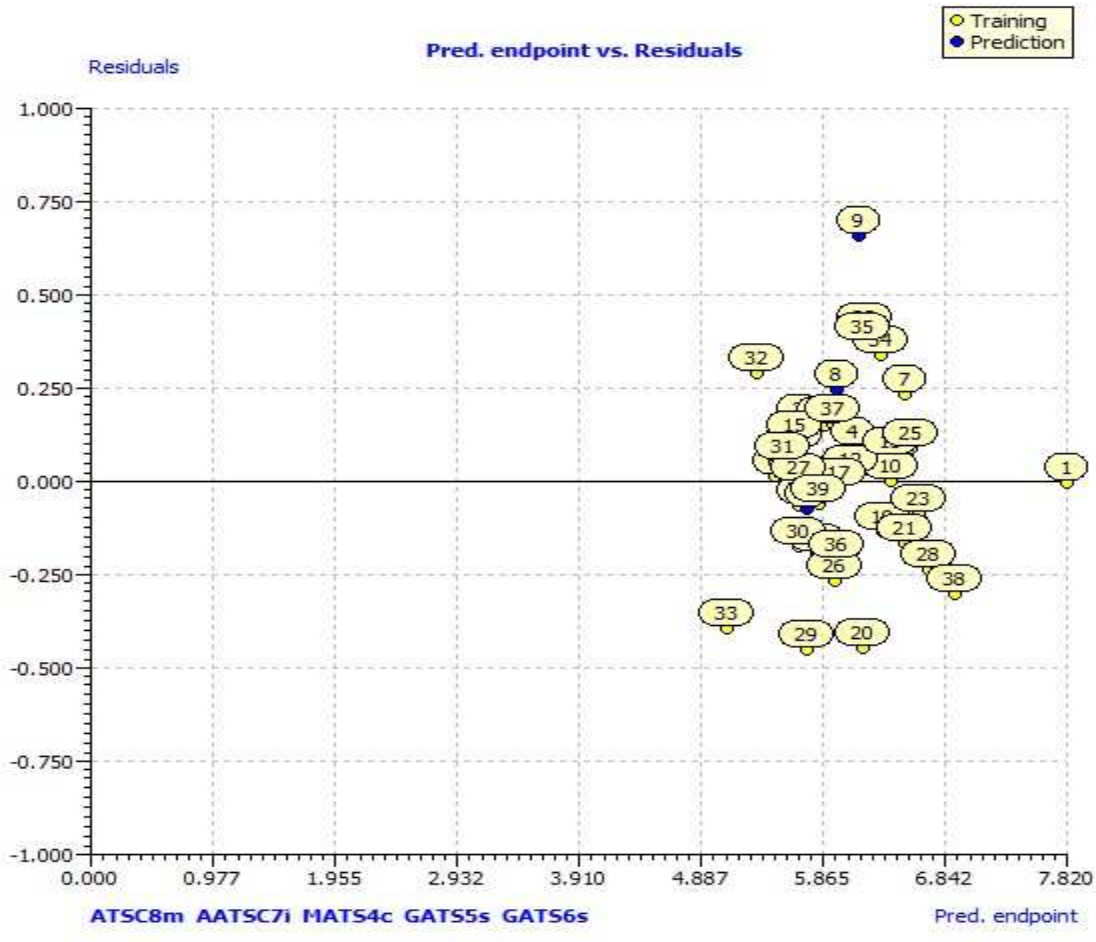


Figure 2. Experimental pIC_{50} values versus residuals for the hydroxyethylamine derivatives predicted by the GA-MLR model

Furthermore, to verify that the model performance was not due to chance, a Y-randomization test was carried out (Figure 4). The randomized models gave much lower R^2 and Q^2 values than the original model, and the obtained modified coefficient of determination (cR^2_p) value was above 0.50, supporting the robustness and reliability of the model. Based on the dataset analysis and QSAR model predictions, Compound 1 was identified as the most suitable template for future lead optimization and drug design. It showed the highest experimental inhibitory activity (pIC_{50} = 7.8239), with an almost identical predicted value (pIC_{50} = 7.8199) and a very low residual error (− 0.0040). In addition, Williams plot analysis (Figure 3) showed that Compound 1 has relatively high leverage (h = 0.480) close to the warning limit (h^* = 0.581), while remaining within the ± 3.0 applicability domain, indicating that it is an influential and reliable lead structure for the hydroxyethylamine derivatives series.

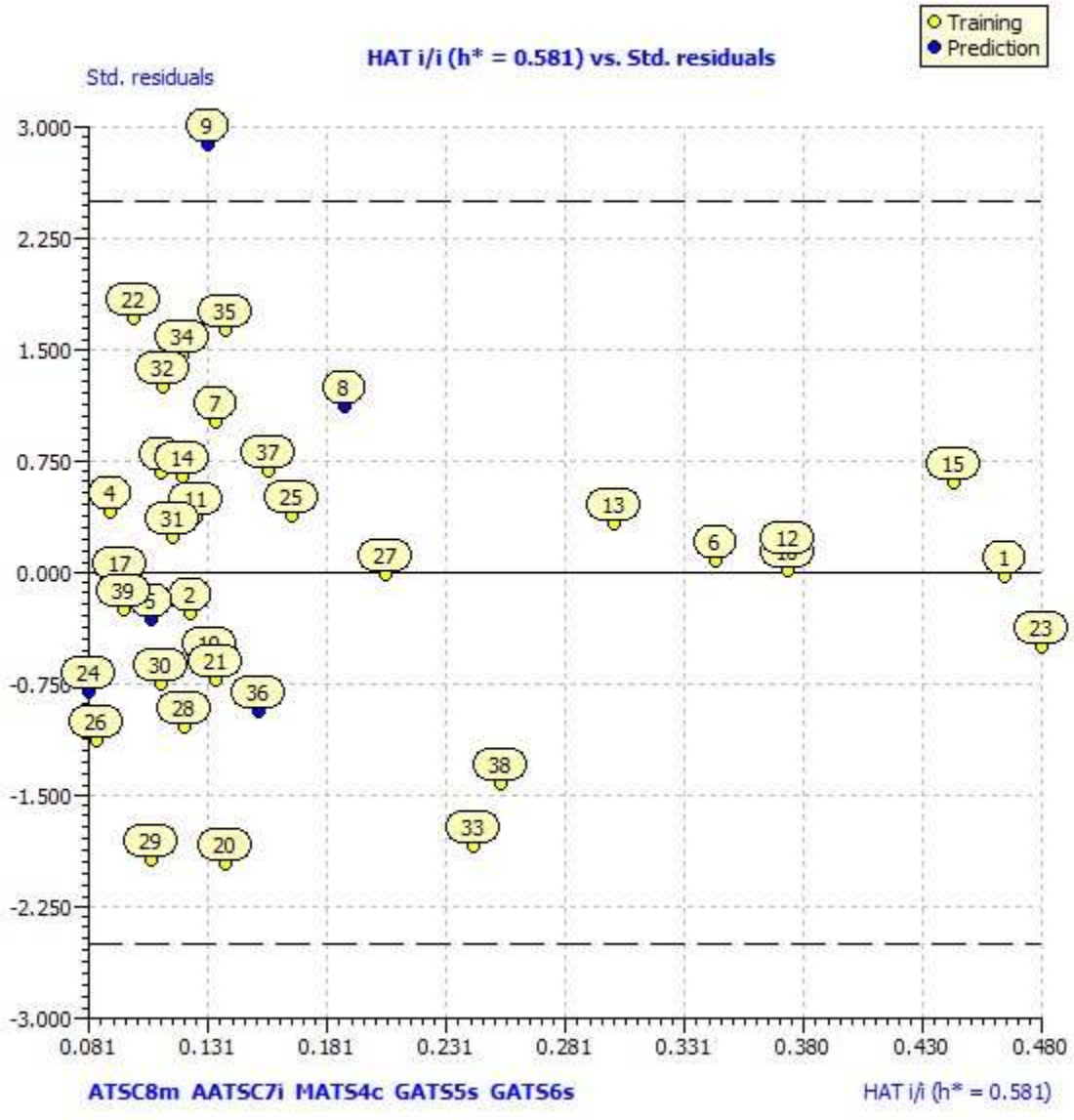


Figure 3. Williams plot (standardized residuals vs leverage) for the QSAR model compounds

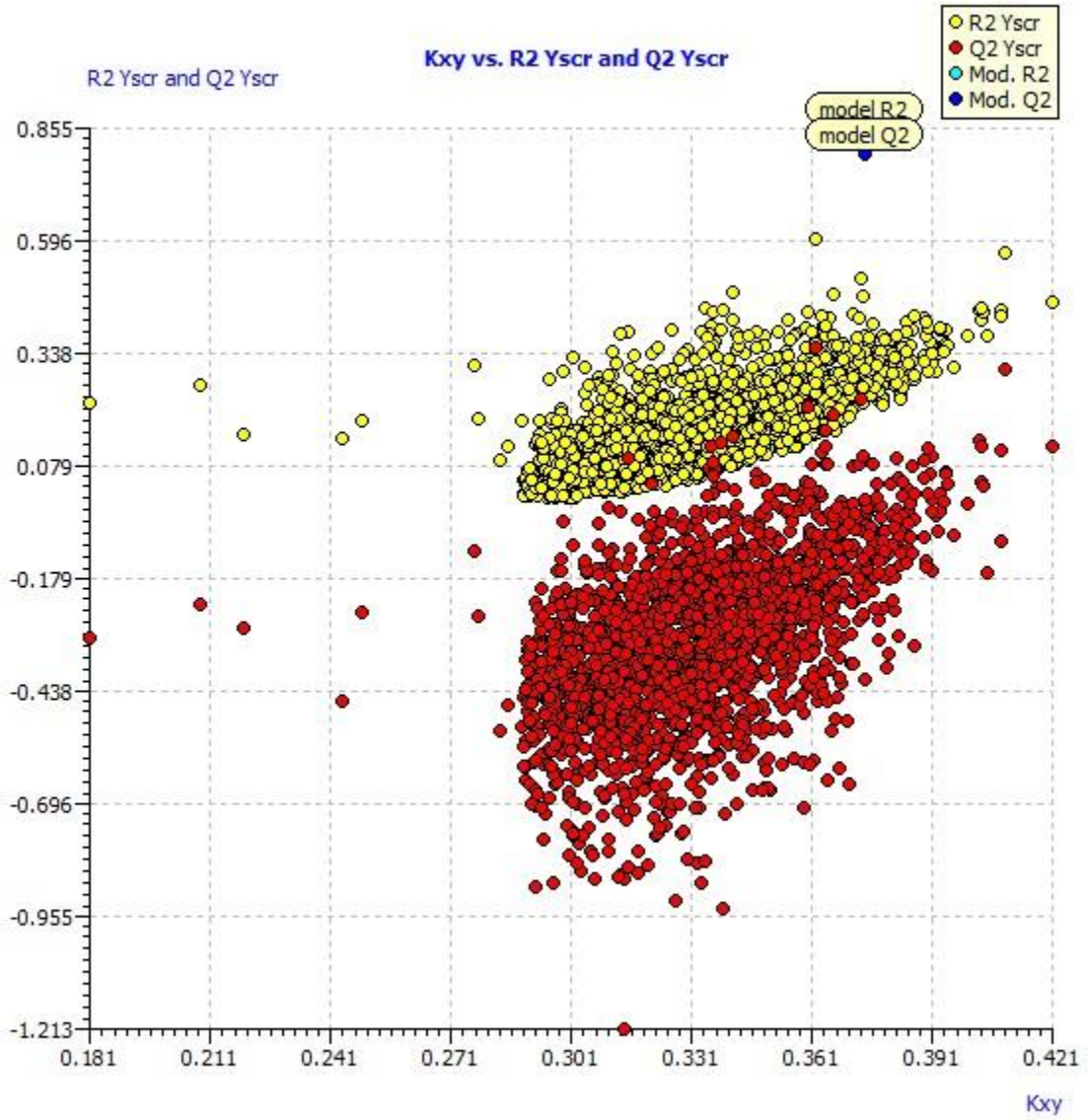


Figure 4. Y-scrambling plot showing the distribution of R^2 and Q^2 values for randomized models compared with the original QSAR model

3.2. In silico screening and docking analysis

Molecular docking analysis of the hydroxyethylamine derivatives was performed to evaluate the binding behavior of the compounds against four target proteins: BACE1 (PDB ID: 2ZHV), AChE (PDB ID: 4EY7), D2 dopamine receptor (PDB ID: 6CM4), and FGFR3 (PDB ID: 6LVM). This approach helps predict how well a ligand fits into the active site of a receptor and estimates its binding affinity, making it a useful and cost-effective tool for virtual screening. In this study, three reference drugs, namely donepezil, galantamine, and rivastigmine, were also docked against the selected Alzheimer's disease targets for comparison. The docking results obtained using EasyDockVina are presented in Table 4. The binding affinities of the reference

drugs against BACE1 were −6.945, −6.773, and −5.321 kcal/mol, respectively; against AChE, they were −11.86, −10.62, and −8.129 kcal/mol, respectively; against D2 dopamine receptor, −9.97, −7.433, and −7.289 kcal/mol, respectively; and against FGFR3, −8.84, −8.306, and −6.592 kcal/mol, respectively.

Among the screened molecules including the reference drugs, compound 10 displayed the most favorable binding profile across all four receptors, with binding affinities of –7.749, –11.54, –11.15, and –9.535 kcal/mol for BACE1, AChE, D2 Dopamine, and FGFR3, respectively. Compound 38 (with binding affinities of –7.828, –11.93, –10.42, and –8.68 kcal/mol for BACE1, AChE, D2 Dopamine, and FGFR3, respectively) and Compound 21 (with binding affinities of –7.696, –11.47, –10.66 and –9.021 kcal/mol for BACE1, AChE, D2 Dopamine, and FGFR3, respectively) also showed notable binding scores, but compound 10 consistently ranked highest overall. Based on these results, compound 10 was selected as the most promising hit compound for further investigation.

Table 4

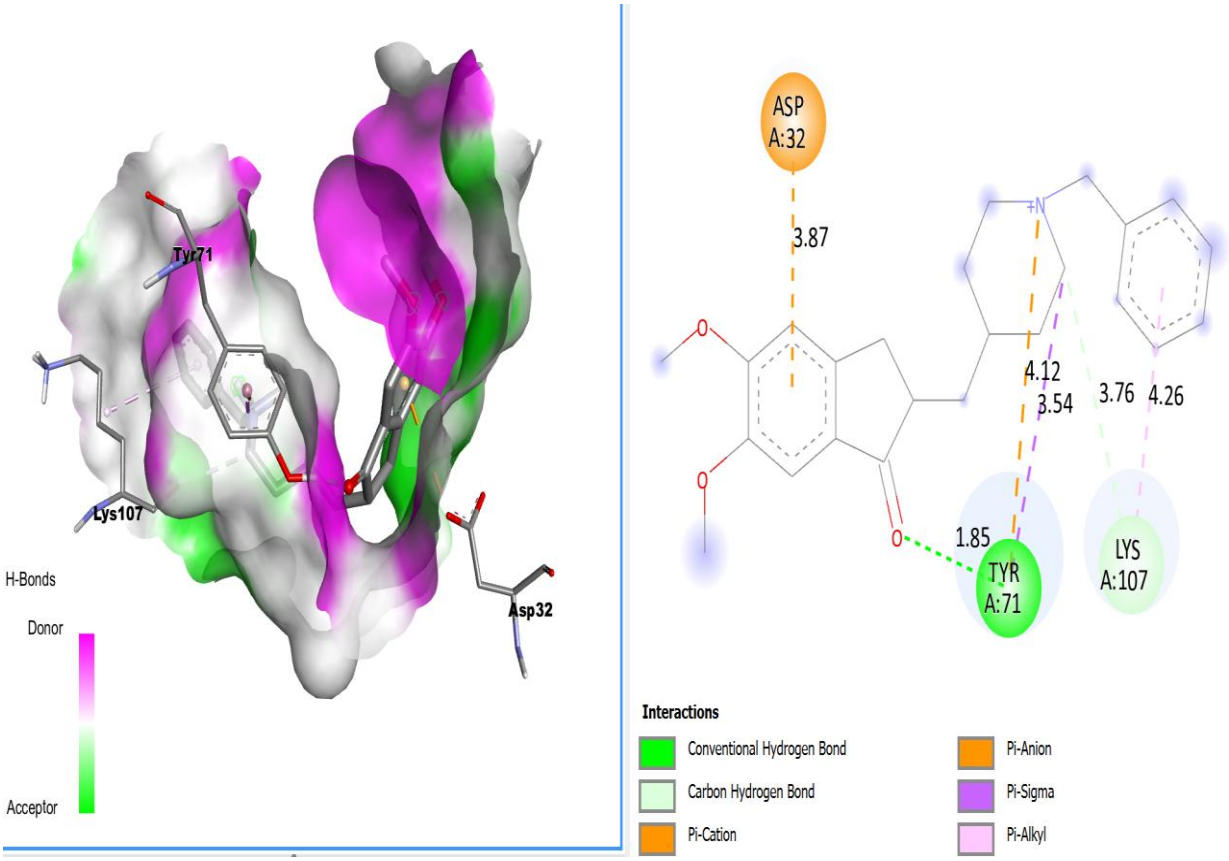
Docking scores of the identified compounds against BACE1 (PDB ID: 2ZHV), AChE (PDB ID: 4EY7), D2 dopamine receptor (PDB ID: 6CM4), and FGFR3 (PDB ID: 6LVM).

Compound ID	Binding affinities (kcal/mol)			
	2ZHV	4EY7	6CM4	6LVM
1	-6.019	-8.758	-8.564	-7.24
2	-7.106	-11.25	-10.09	-8.472
3	-7.567	-11.14	-9.395	-8.539
4	-7.404	-10.74	-9.596	-8.644
5	-7.094	-11.88	-10.57	-8.709
6	-7.72	-11.68	-10.75	-8.327
7	-7.118	-11.64	-10.65	-8.574
8	-6.592	-11.21	-10.76	-8.329
9	-7.469	-10.48	-8.852	-7.982
10	-7.749	-11.54	-11.15	-9.535
11	-7.823	-10.07	-8.587	-8.107
12	-7.548	-9.769	-8.831	-8.365
13	-8.105	-12.01	-9.69	-8.41
14	-7.747	-11.3	-10.44	-8.925
15	-6.357	-10.72	-9.865	-7.975
16	-7.443	-11.05	-10.15	-8.293
17	-7.589	-10.35	-9.406	-8.496
18	-7.299	-10.21	-9.011	-8.591
19	-7.315	-11.08	-9.526	-9.064
20	-7.238	-10.89	-9.895	-8.9
21	-7.696	-11.47	-10.66	-9.021

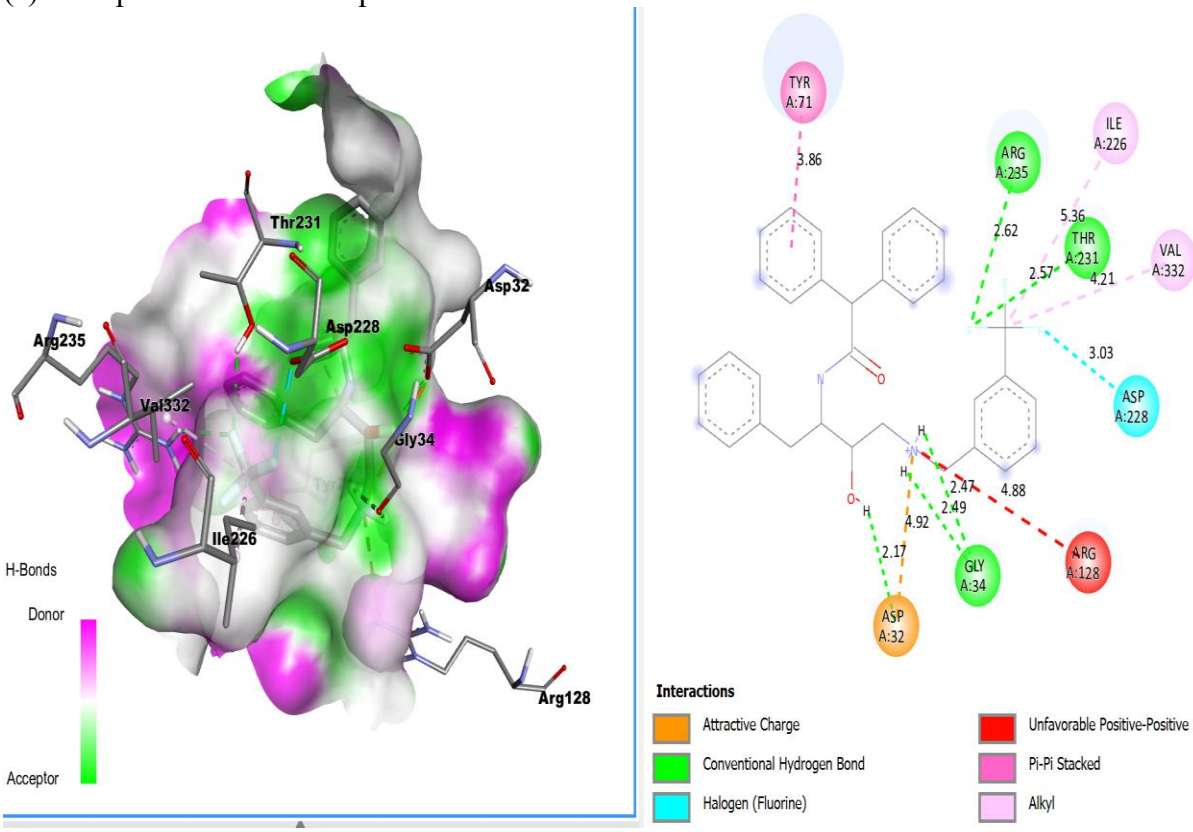
22	-8.046	-11.29	-9.775	-8.78
23	-7.169	-10.12	-8.443	-7.983
24	-7.503	-10.69	-9.768	-8.303
25	-7.604	-10.33	-8.407	-8.418
26	-6.895	-9.945	-8.656	-7.744
27	-6.908	-10.48	-10.05	-7.68
28	-7.378	-10.9	-9.366	-8.868
29	-8.313	-10.82	-9.438	-7.858
30	-7.89	-10.88	-9.469	-8.489
31	-8.094	-10.28	-8.444	-7.842
32	-8.027	-11.43	-10.01	-7.866
33	-8.004	-11.55	-9.961	-8.586
34	-7.036	-10.61	-8.922	-8.395
35	-8.061	-10.78	-9.989	-9.49
36	-7.394	-11.75	-10.28	-8.43
37	-7.662	-10.95	-10.36	-8.191
38	-7.828	-11.93	-10.42	-8.68
39	-7.406	-10.98	-9.906	-8.028
Donepezil	-6.945	-11.86	-9.97	-8.84
Galantamine	-6.773	-10.62	-7.433	-8.306
Rivastigmine	-5.321	-8.129	-7.289	-6.592

3.3. Molecular docking with BACE1 inhibitor (PDB ID: 2ZHV)

The binding modes of the reference drug, donepezil, and the top-ranked candidate, compound 10, within the active site of the BACE1 receptor are shown in Figures 5a and 5b, respectively. In the reference complex, donepezil fits well into the binding pocket of BACE1 and is stabilized by several interactions, including a Pi-anion interaction with ASP32, Pi-sigma and Pi-alkyl interactions with PHE108 and LYS107, a conventional hydrogen bond with TYR71, and additional van der Waals contacts with ASP228, THR231, GLY230, GLY34, SER35, ILE118, and GLY74. Compound 10 showed a more extensive interaction pattern within the BACE1 binding site. The complex was stabilized by an attractive charge interaction with ASP32, a halogen bond with ASP228, Pi-Pi stacking with TYR71, alkyl interactions with VAL332 and ILE226, and multiple conventional hydrogen bonds with GLY34, SER35, THR231, and ARG235. Additional van der Waals interactions with GLY230, ILE110, TRP115, LEU30, LYS107, GLY74, TYR198, and THR329 further supported the binding. Although a minor unfavorable interaction was observed with ARG128, the overall interaction profile suggests that compound 10 has stronger binding potential than donepezil and may serve as a promising inhibitor candidate for Alzheimer's disease targets.



(a) Donepezil–BACE1 complex

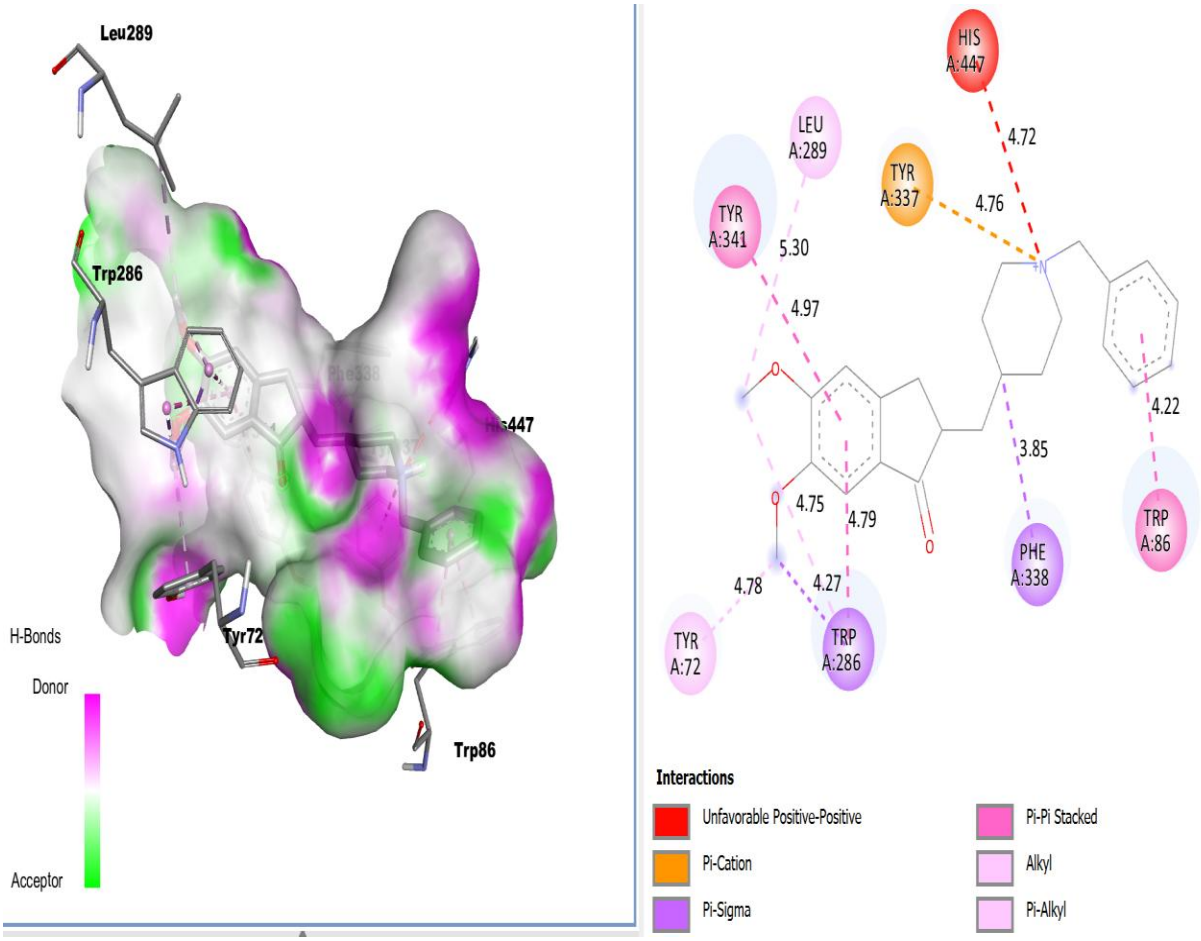


(b) Ligand 10–BACE1 complex

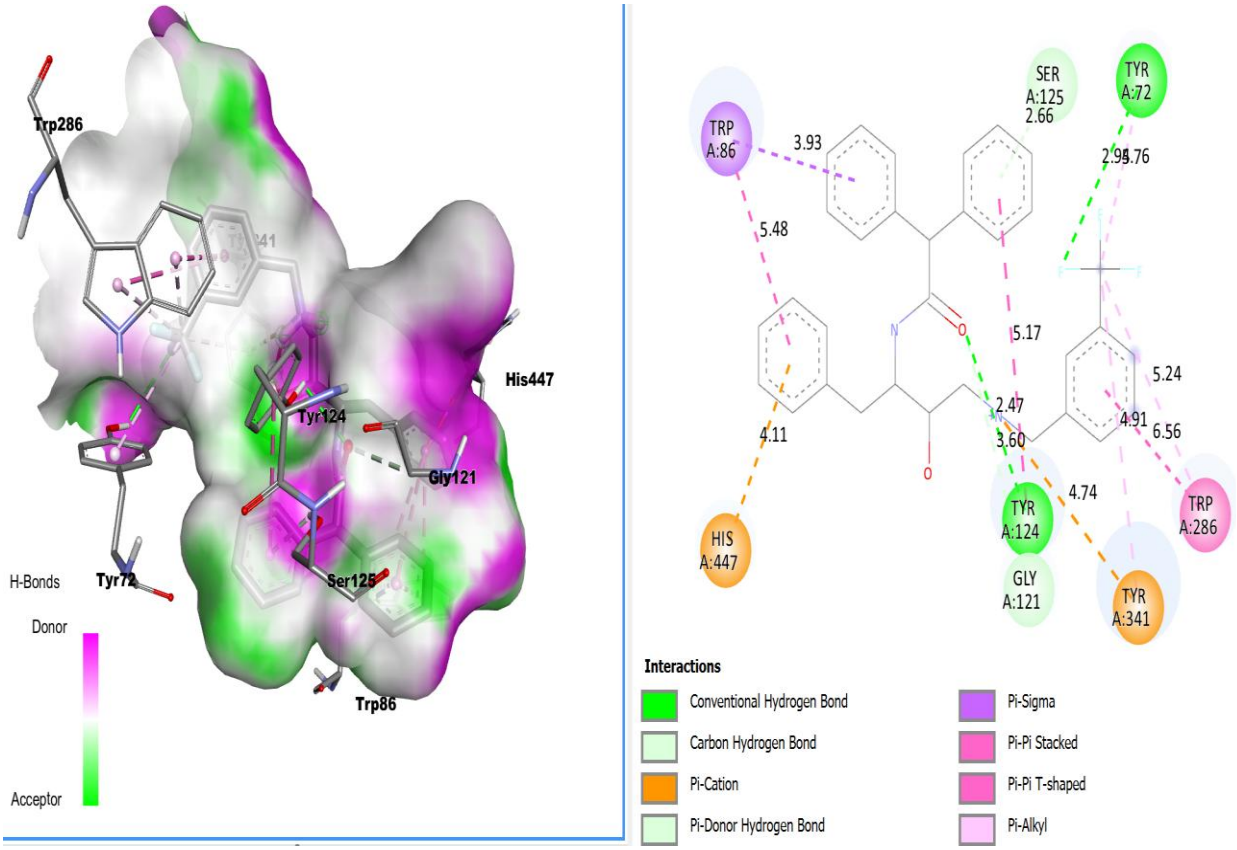
Figure 5. Protein–ligand interactions of (a) donepezil, the reference drug, and (b) ligand 10 with the BACE1 inhibitor (PDB ID: 2ZHV).

3.4. Molecular docking with AChE inhibitor (PDB ID: 4EYZ)

Figures 6a and 6b show the binding modes of the reference drug, donepezil, and the top-ranked candidate, compound 10, within the active site of the AChE receptor, respectively. In the reference complex, donepezil fits well into the binding pocket and is stabilized by several interactions, including an unfavorable positive-positive interaction with HIS447, a Pi-cation interaction with TYR337, Pi-sigma and Pi-pi stacking interactions with TRP286 and TYR341, as well as alkyl and Pi-alkyl interactions with LEU289, PHE338, TRP86, TYR72, and TYR341. Additional stabilization is provided by carbon-hydrogen bonds with TYR124 and the methoxy oxygen atoms, while SER293, PHE295, GLY121, TYR133, GLY120, and SER203 contribute through van der Waals interactions.



(a) Donepezil–AChE complex



(b) Ligand 10–AChE complex

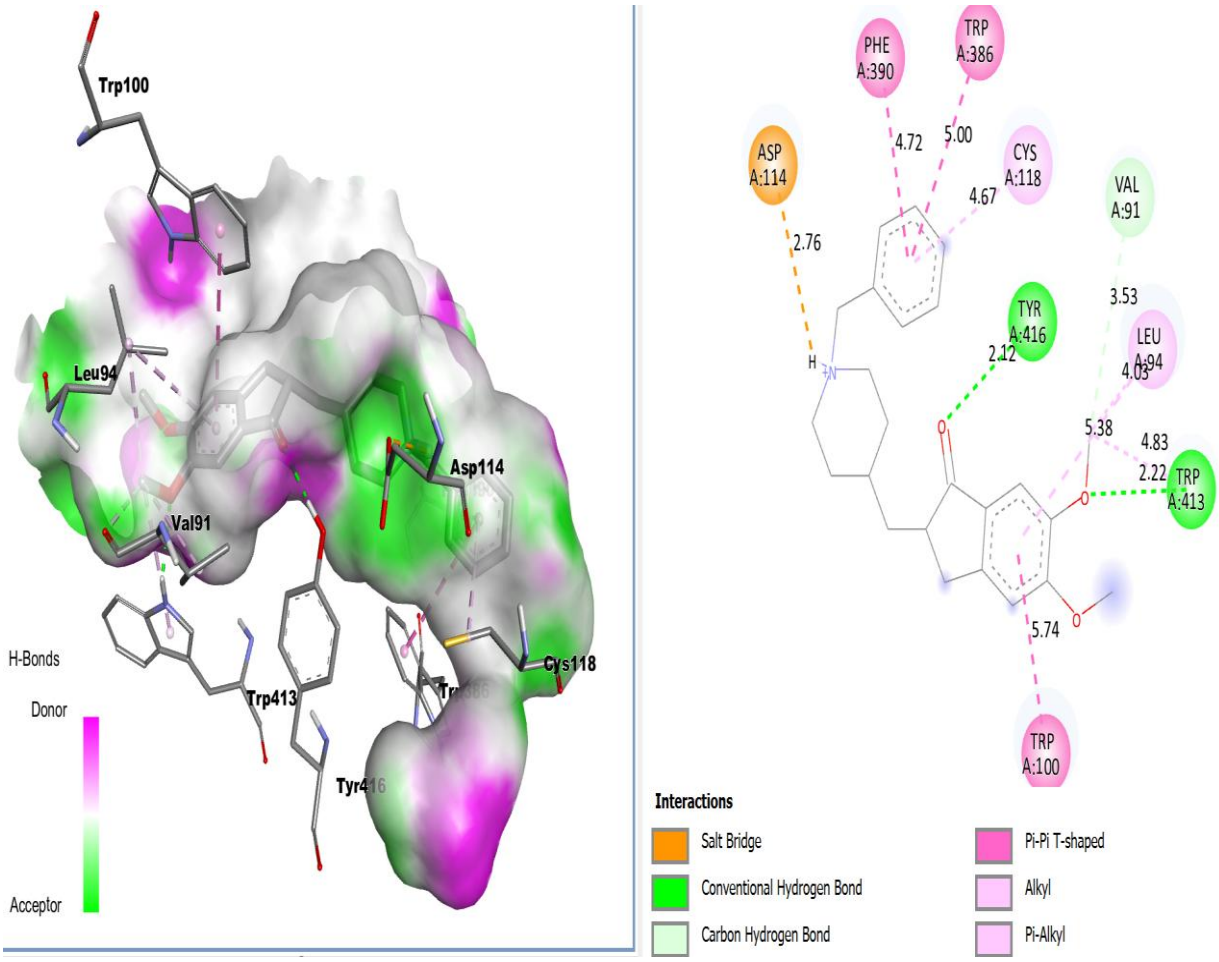
Figure 6. Protein–ligand interactions of (a) donepezil, the reference drug, and (b) ligand 10 with the AChE inhibitor (PDB ID: 4EYZ).

Compound 10 showed a more extensive interaction network within the AChE active site. The complex is stabilized by Pi-cation interactions with HIS447 and TYR341, Pi-sigma and Pi-pi stacking interactions with TRP86 and TRP286, and Pi-alkyl interactions with TRP86. In addition, the ligand forms conventional hydrogen bonds with TYR72, TYR124, and SER125, a Pi-donor hydrogen bond with TYR124, and a carbon-hydrogen bond with ASP74. Further stabilization is contributed by van der Waals interactions with GLU202, SER203, TYR133, LEU130, GLY126, ALA127, ASN87, GLN71, PHE295, PHE297, GLY121, GLY120, GLY448, and TYR337.

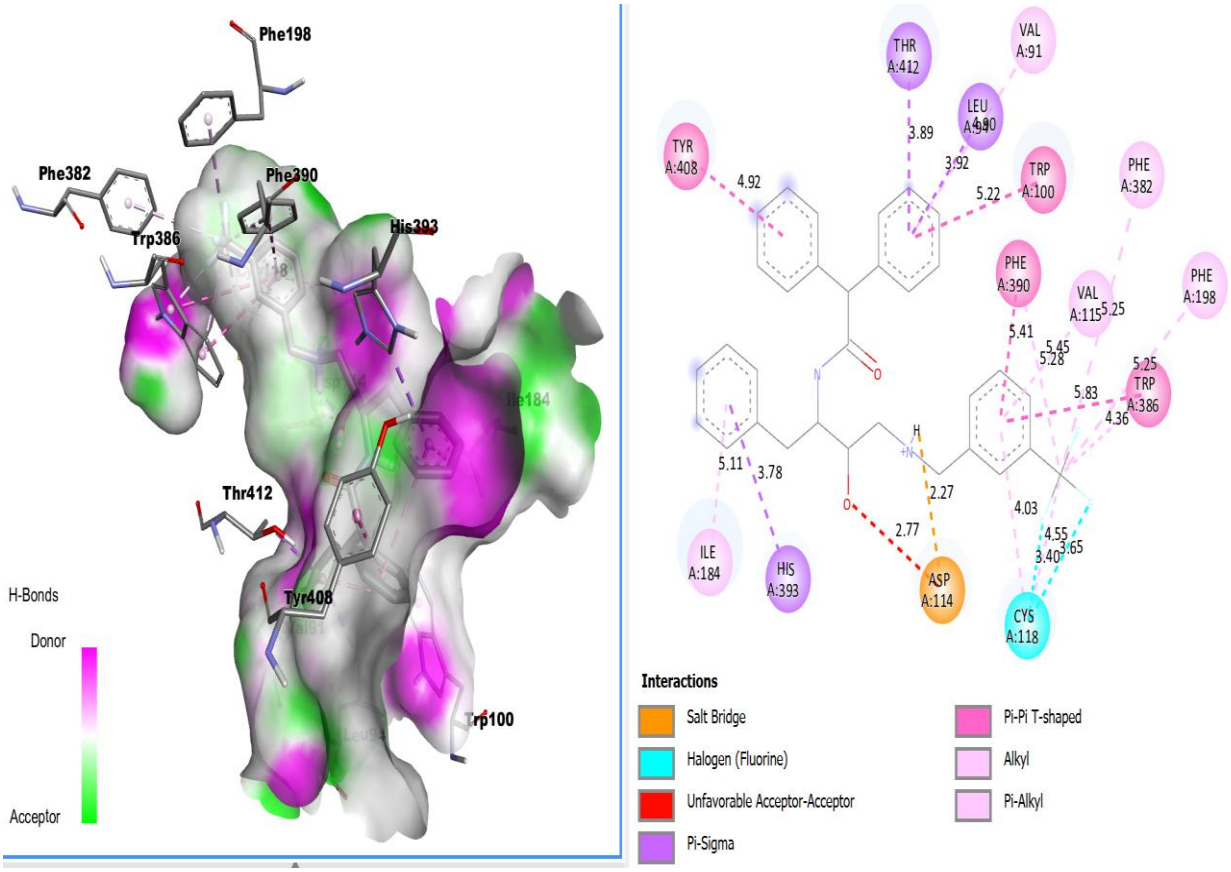
3.5. Molecular docking with D2 Dopamine receptor (PDB ID: 6CM4)

The binding orientations of the reference drug, donepezil, and compound 10 in the D2 dopamine receptor are presented in Figures 7a and 7b. Donepezil occupies the receptor pocket through a combination of electrostatic, hydrophobic, and hydrogen-bonding interactions. A salt bridge is observed between the protonated nitrogen atom and ASP114, while Pi-Pi T-shaped interactions with TRP386, PHE390, and TRP100, together with alkyl and Pi-alkyl contacts involving CYS118, VAL115, LEU94, and VAL91, help stabilize the complex. Additional support comes from hydrogen bonds with TRP413 and carbon-hydrogen interactions with THR412 and

TRP413, as well as van der Waals contacts with SER197, SER193, PHE389, TYR416, PHE189, and SER409. Compound 10 exhibited a broader interaction network in the same receptor site. Its binding was reinforced by a salt bridge with ASP114 and several halogen bonds with CYS118, which may enhance binding specificity. The ligand also formed Pi-Sigma, Pi-Pi T-shaped, alkyl, and Pi-alkyl interactions with LEU94, TRP386, PHE390, TYR408, TRP100, PHE198, VAL115, ILE184, HIS393, VAL91, and THR412. Although an unfavorable acceptor-acceptor interaction was observed with ASP114, the overall complex was further supported by van der Waals contacts with SER197, PHE382, SER193, THR119, VAL190, PHE110, PHE389, TYR416, and PHE189.



(a) Donepezil–D2 Dopamine complex



(b) Ligand 10–D2 Dopamine complex

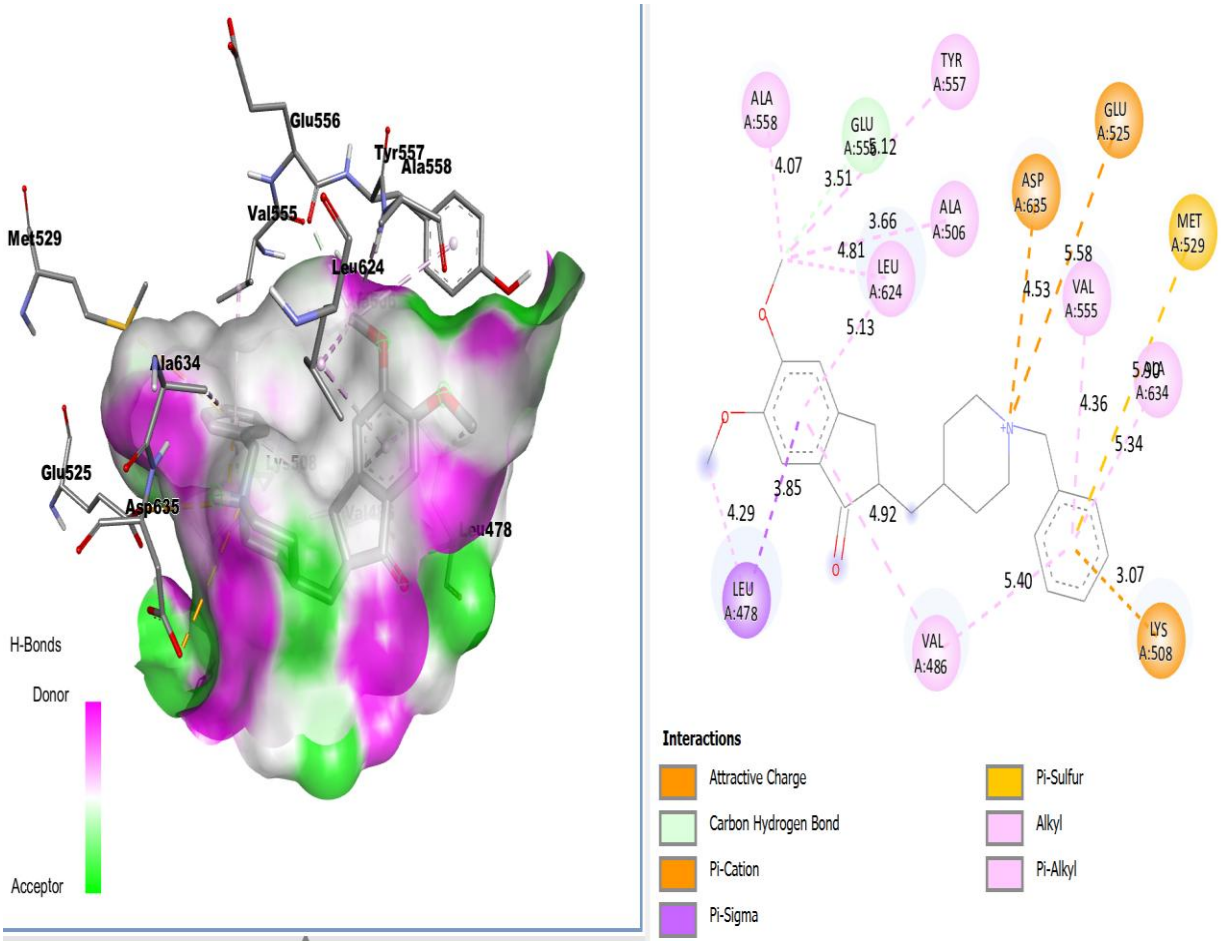
Figure 7. Protein–ligand interactions of (a) donepezil, the reference drug, and (b) ligand 10 with the D2 Dopamine receptor (PDB ID: 6CM4).

3.6. Molecular docking with FGFR3 receptor (PDB ID: 6LVM)

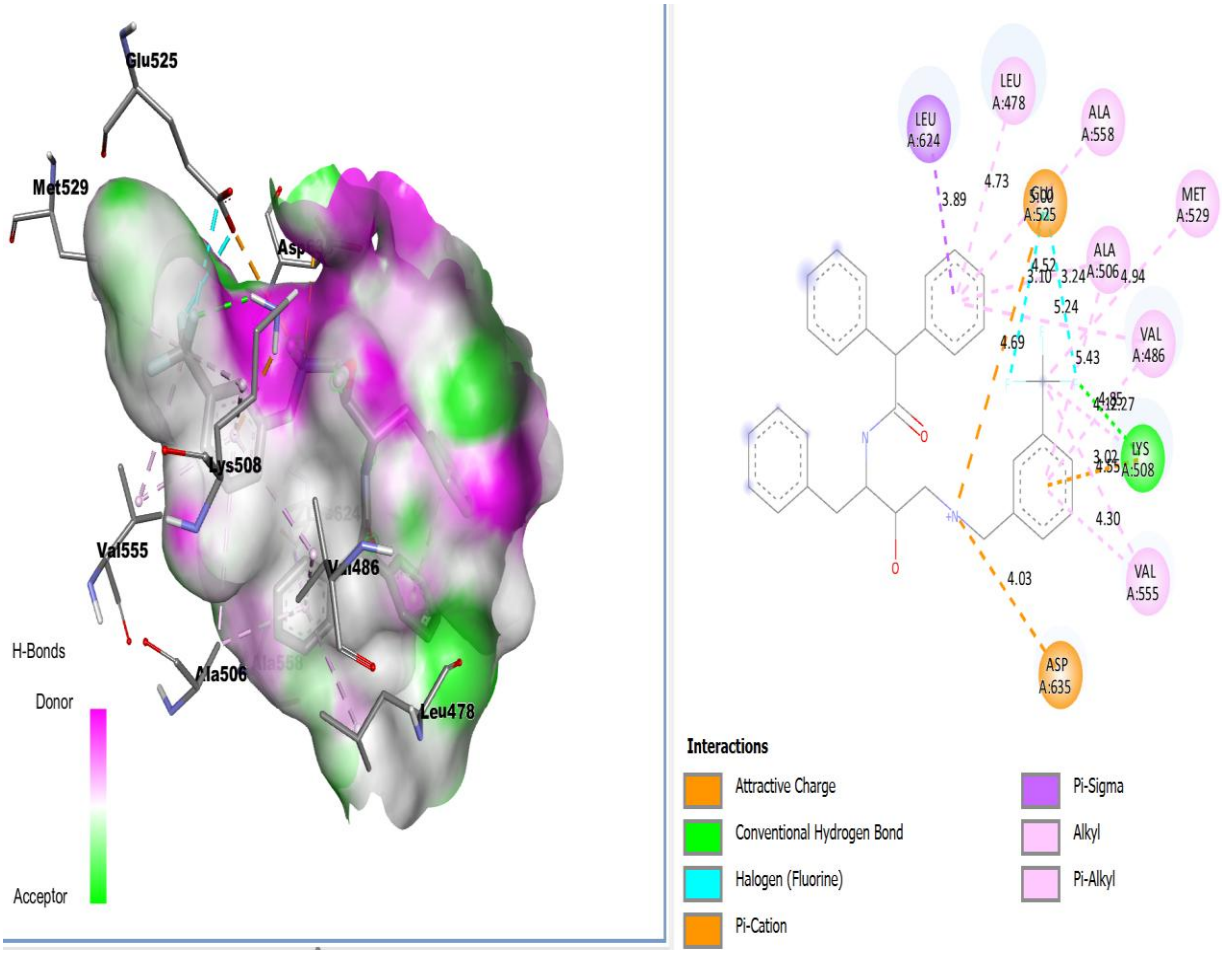
The binding modes of the reference drug, donepezil, and compound 10 within the active site of the FGFR3 receptor are shown in Figures 8a and 8b, respectively. The reference complex, donepezil, fits well into the binding pocket of FGFR3 and is stabilized by several interactions. In particular, an attractive charge interaction with ASP635 (3.93 Å), together with Pi-cation and Pi-anion contacts involving LYS508 (5.41 Å) and GLU525 (8.99 Å), contributes to electrostatic stabilization. Hydrophobic interactions are also observed through a Pi-sigma interaction with LEU478 (4.23 Å), as well as alkyl and Pi-alkyl interactions with LEU478 (4.52 Å), VAL486 (6.29 Å and 6.46 Å), ALA558 (3.73 Å), LEU624 (5.44 Å and 5.99 Å), VAL555, and ALA634 (5.14 Å and 6.01 Å). In addition, the ligand forms carbon-hydrogen bonds with GLU556 (4.50 Å, 4.62 Å, and 6.54 Å) and TYR557, while ASN622, ALA506, GLY561, and GLY479 contribute through van der Waals interactions. These multiple contacts support the stability of the reference drug within the receptor active site.

The binding orientation of compound 10 was similarly examined in the FGFR3 receptor active site, and it displayed a more extensive interaction network than the reference drug. The

complex was mainly stabilized by an attractive charge interaction with ASP635 (3.71 Å) and a Pi-cation interaction with GLU525 (5.68 Å). In addition, several halogen (fluorine) bonds were formed with ALA506 (4.68 Å), PHE636 (5.73 Å and 6.82 Å), and LYS508 (4.51 Å), which may enhance binding specificity. The hydrophobic region of the complex was stabilized by Pi-sigma, alkyl, and Pi-alkyl interactions with LEU624 (5.18 Å), TYR557 (5.15 Å), ALA558, MET529 (6.15 Å), VAL486, LYS508 (4.83 Å and 5.33 Å), and VAL555 (6.07 Å). The ligand also formed a conventional hydrogen bond with LYS508 (4.13 Å). Further stabilization was provided by van der Waals interactions with ASN562, VAL553, GLY479, GLU480, GLY481, ALA634, and GLY484. Overall, the combination of electrostatic, hydrophobic, halogen-bonding, and hydrogen-bonding interactions suggests that compound 10 has stronger binding affinity and greater stability than the reference drug.



(a) Donepezil–FGFR3 complex



(b) Ligand 10–FGFR3 complex

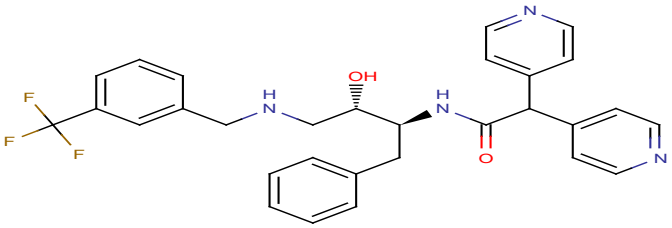
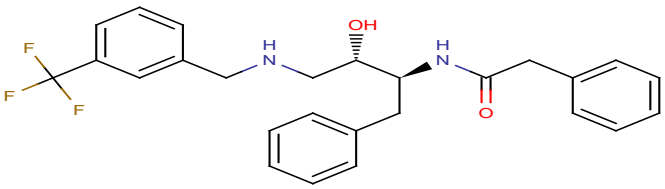
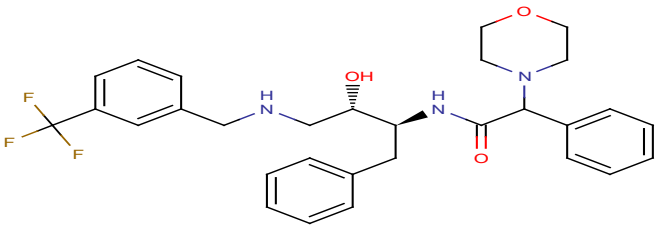
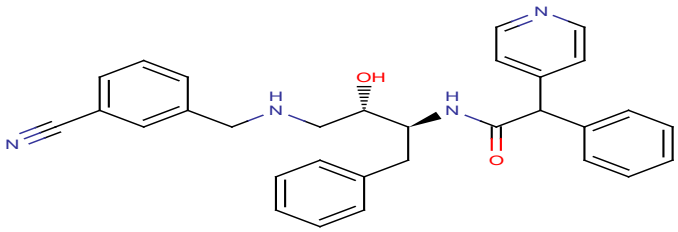
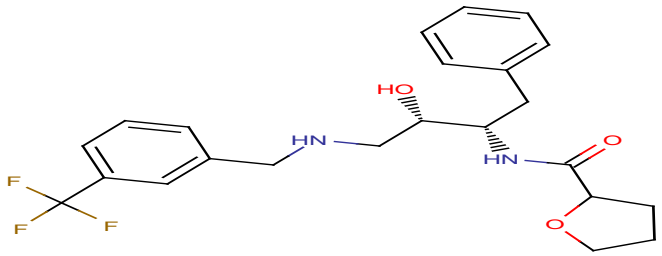
Figure 8. Protein–ligand interactions of (a) donepezil, the reference drug, and (b) ligand 10 with the FGFR3 receptor (PDB ID: 6LVM).

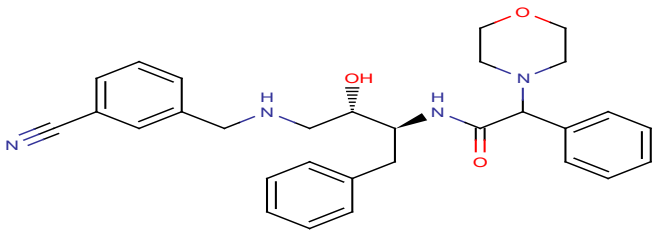
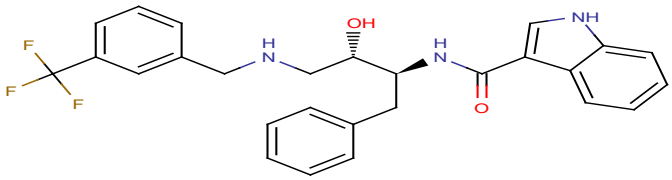
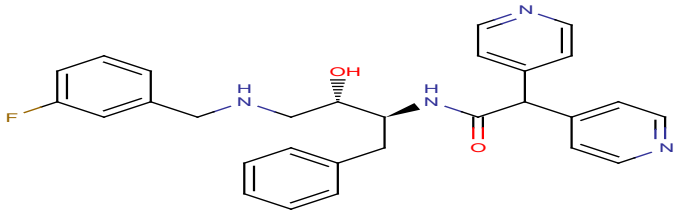
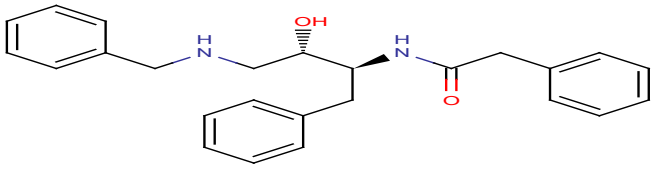
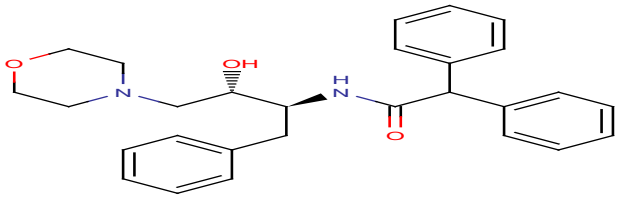
3.7. Design and molecular docking of novel analogs of ligand 10

To explore improved pharmacological profiles, structural analogs of compound 10 were systematically designed by modifying substituents and incorporating key pharmacophoric fragments (Table 5). The 3D structures of these novel analogs were generated in MarvinSketch and energy-minimized according to the procedure reported by Hanwell *et al*. (2012), as done for the original dataset. The SMILES notation (Supplementary Table 2) were converted and save in SD file for subsequent docking and validation studies. The in silico synthesized analogs were compared with reference drugs and the template compound 10, and some of the designed analogs showed better binding affinities than both the template compound and the reference standards across the four target receptors, with binding free energies ranging from −6.771 to −11.85 kcal/mol. Among the series, Ligands B1 and B2 gave the most favorable docking scores, whereas B9 and B6 showed the lowest average binding affinities.

Table 5

Molecular structure and binding affinity of the newly designed ligand.

Designed ligand ID	Molecular structure	Binding affinities (kcal/mol)			
		2ZHV	4EY7	6CM4	6LVM
B1		-7.949	-11.5	-10.3	-9.149
B2		-7.206	-11.3	-10.72	-8.854
B3		-7.55	-11.19	-9.001	-8.385
B4		-6.775	-11.25	-10.03	-8.83
B5		-7.298	-11.2	-9.698	-8.789

B6		-7.074	-10.84	-9.607	-8.04
B7		-7.786	-11.4	-9.559	-8.567
B8		-7.869	-10.93	-9.624	-9.15
B9		-6.771	-11.15	-10.04	-8.041
B10		-7.563	-10.08	-9.036	-9.345

3.8. Physicochemical, bioavailability, and drug-likeness profiles

The SwissADME (www.swissadme.ch) was used to predict physicochemical parameters and ADME-related properties of the designed analogs, the template Compound 10, and the reference drug Donepezil, as summarized in Table 6. According to Lipinski's Rule of Five (Ro5) a standard benchmark for evaluating oral bioavailability, a candidate molecule should ideally violate no more than one of the following criteria: molecular weight (MW) < 500 g/mol, hydrogen bond acceptors (HBA) < 10, hydrogen bond donors (HBD) < 5, and lipophilicity (MLogP) < 4.15 (Lipinski *et al*., 2001). Among the evaluated compounds, eight of the ten designed analogs (B2, B4, B5, B6, B7, B8, B9, and B10) exhibited zero Lipinski violations, while analogs B1 and B3

displayed only one minor violation (MW > 500 g/mol). In contrast, the parent template (Compound 10) violated two criteria (MW > 500 g/mol and MLogP > 4.15).

Table 6

Physicochemical and bioavailability properties of the designed analogs, compound 10, and donepezil

ID name	MW < 500	HBA ≤ 10	HBD ≤ 5	MLOGP ≤ 4.15	TPSA ≤ 140	Lipinski Ro5	ESol Log S	BBB Permeant	B.S Higher the better	S.A Lower the better
B1	534.57	8	3	2.6	87.14	1	-5.3	No	0.55	4.04
B2	456.5	6	3	4.08	61.36	0	-5.11	Yes	0.55	3.66
B3	541.6	8	3	2.81	73.83	1	-5.38	Yes	0.55	4.51
B4	490.6	5	3	2.17	98.04	0	-5.06	No	0.55	4.2
B5	436.47	7	3	2.47	70.59	0	-4.19	Yes	0.55	3.88
B6	498.62	6	3	1.39	97.62	0	-4.47	No	0.55	4.41
B7	481.51	6	4	3.44	77.15	0	-5.49	No	0.55	3.73
B8	484.56	6	3	2.22	87.14	0	-4.6	No	0.55	3.83
B9	388.5	3	3	3.3	61.36	0	-4.25	Yes	0.55	3.31
B10	444.57	4	2	2.68	61.8	0	-4.8	Yes	0.55	3.86
Compd. 10	532.6	6	3	5	61.36	2	-6.63	No	0.17	4.15
Donepezil	379.49	4	0	3.06	38.77	0	-4.81	Yes	0.55	3.36

MW = molecular weight in g/mol, HBA = hydrogen bond acceptor, HBD = hydrogen bond donor, MlogP = lipophilicity, TPSA = total polar surface area, BBB = blood-brain barrier permeant, B.S = bioavailability score, and S.A = synthetic accessibility, ESOL = estimated water solubility.

All designed analogs displayed Topographical Polar Surface Area (TPSA) values well below the 140 Å² threshold (ranging from 61.36 to 98.04 Å²), indicating favorable human intestinal absorption (HIA) upon oral administration. Regarding aqueous solubility (ESOL Log S), all newly designed analogs exhibited moderate solubility (ranging from -4.19 to -5.49), representing a substantial improvement over the poorly soluble template Compound 10 (Log S = -6.63). For central nervous system (CNS) targets such as Alzheimer's disease, blood-brain barrier (BBB) penetration is essential (Thai *et al*., 2020). Analogs B2, B3, B5, B9, and B10 were predicted to be BBB permeant, mirroring the behavior of the reference drug Donepezil, whereas the parent Compound 10 failed to cross the BBB. Synthetic Accessibility (SA) scores ranged from 3.31 (B9) to 4.51 (B3). Since lower SA scores denote ease of chemical synthesis, compounds B2 (3.66), B5 (3.88), and B9 (3.31) were predicted to be synthetically accessible with lower synthetic rigor than the template (4.15), whereas B3 (4.51) and B6 (4.41) present slightly higher synthetic complexity. To gain a rapid visual assessment of drug-likeness, oral bioavailability radars (Ugbe *et al*., 2023c) for the top-performing candidate compounds (B2 and B5) are depicted in Figure 9. The pink hexagonal region defines the optimal physicochemical space across six key properties: size, lipophilicity (LIPO), solubility (INSOLU), polarity (POLAR), saturation (INSATU), and flexibility (FLEX). Both B2 and B5 reside almost entirely within the ideal drug-like envelope,

exhibiting only a mild off-axis deviation in molecular flexibility (FLEX) (Daina *et al*., 2017; Veber *et al*., 2002).

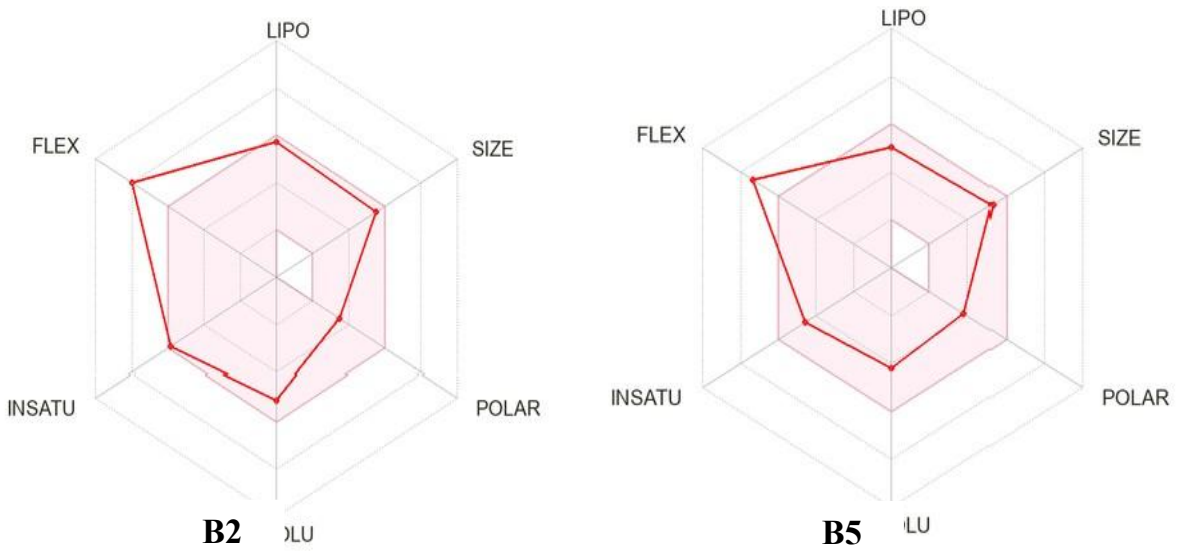


Figure 9. Oral bioavailability radars of compounds B2 and B5.

3.9. In silico pharmacokinetic and ADMET profiling

The pkCSM (biosig.lab.uq.edu.au/pkcsm) was employed to further evaluate the therapeutic potential and safety margin of the designed analogs, template compound 10, and reference drugs donepezil, with an in silico assessment of Absorption, Distribution, Metabolism, Excretion, and Toxicity (ADMET) as indicated in Table 7. High human intestinal absorption (HIA) was predicted for all analogs, with B10 (95.68%), B8 (93.55%), and B9 (92.40%) showing particularly strong permeability, comparable to donepezil (93.74%). Blood-brain barrier penetration, a key requirement for Alzheimer's disease therapeutics, was evaluated using predicted LogBB values: B2 (LogBB = 0.129) and B9 (LogBB = 0.122) exhibited enhanced BBB permeability relative to both donepezil (LogBB = 0.048) and the template compound 10 (LogBB = −0.012). All analogs, compound 10, and donepezil were predicted to be substrates and inhibitors of P-glycoprotein (P-gp I and II), suggesting possible involvement in active efflux transport.

Table 7

ADMET profiles of the designed analogs, compound 10, and donepezil

ADMET Properties	Compounds ID											
	B1	B2	B3	B4	B5	B6	B7	B8	B9	B10	Compd 10	Donepezil
	Absorption											
Human intestinal absorption (%)	89.60	86.21	81.83	82.03	87.23	72.22	85.56	93.55	92.401	95.683	86.75	93.74
Skin permeability	-2.74	-2.76	-2.74	-2.74	-2.80	-2.74	-2.74	-2.74	-2.77	-2.736	-2.74	-2.97
P-glycoprotein substrate	Yes	Yes	Yes	Yes	Yes	Yes	Yes	Yes	Yes	Yes	Yes	Yes

P-glycoprotein I inhibitor	Yes	Yes	Yes	Yes	Yes	Yes	Yes	Yes	Yes	Yes	Yes	Yes
P-glycoprotein II inhibitor	Yes	Yes	Yes	Yes	Yes	Yes	Yes	Yes	Yes	Yes	Yes	Yes
Distribution												
BBB permeability (LogBB)	-1.292	0.129	-0.76	-0.746	-0.975	-0.513	-0.867	-1.163	0.122	-0.246	-0.012	0.048
CNS permeability (Log PS)	-2.672	-2.339	-2.617	-2.494	-2.734	-2.835	-2.199	-2.857	-2.497	-2.593	-2.006	-1.422
Metabolism												
CYP2D6 substrate	Yes	Yes	Yes	Yes	Yes	Yes	Yes	Yes	Yes	Yes	Yes	No
CYP3A4 substrate	Yes	Yes	Yes	Yes	Yes	Yes	Yes	Yes	Yes	Yes	Yes	Yes
CYP1A2 inhibitor	No	No	No	No	No	No	Yes	No	Yes	No	No	No
CYP2C19 inhibitor	Yes	Yes	Yes	Yes	Yes	Yes	Yes	Yes	Yes	Yes	Yes	No
CYP2C9 inhibitor	Yes	Yes	No	Yes	No	No	Yes	Yes	No	Yes	Yes	No
CYP2D6 inhibitor	No	Yes	Yes	Yes	Yes	Yes	Yes	No	Yes	Yes	Yes	Yes
CYP3A4 inhibitor	Yes	Yes	Yes	Yes	Yes	Yes	Yes	Yes	Yes	Yes	Yes	Yes
Excretion												
Total Clearance (Log ml/min/kg)	0.914	0.964	0.801	1.003	1.066	1.006	1.014	1.051	1.171	0.832	0.68	1.006
Renal OCT2 substrate	No	No	No	No	No	No	No	No	No	No	No	Yes
Toxicity												
AMES toxicity	No	No	No	Yes	No	No	No	No	No	No	No	No
Max. tolerated dose (human)	0.687	0.501	0.066	0.543	0.196	0.035	0.708	0.441	0.172	0.336	0.381	0.078
hERG I inhibitor	No	No	No	No	No	No	No	No	No	Yes	No	No
Hepatotoxicity	Yes	Yes	No	Yes	Yes	Yes	Yes	Yes	Yes	No	Yes	No
Skin Sensitization	No	No	No	No	No	No	No	No	No	No	No	No

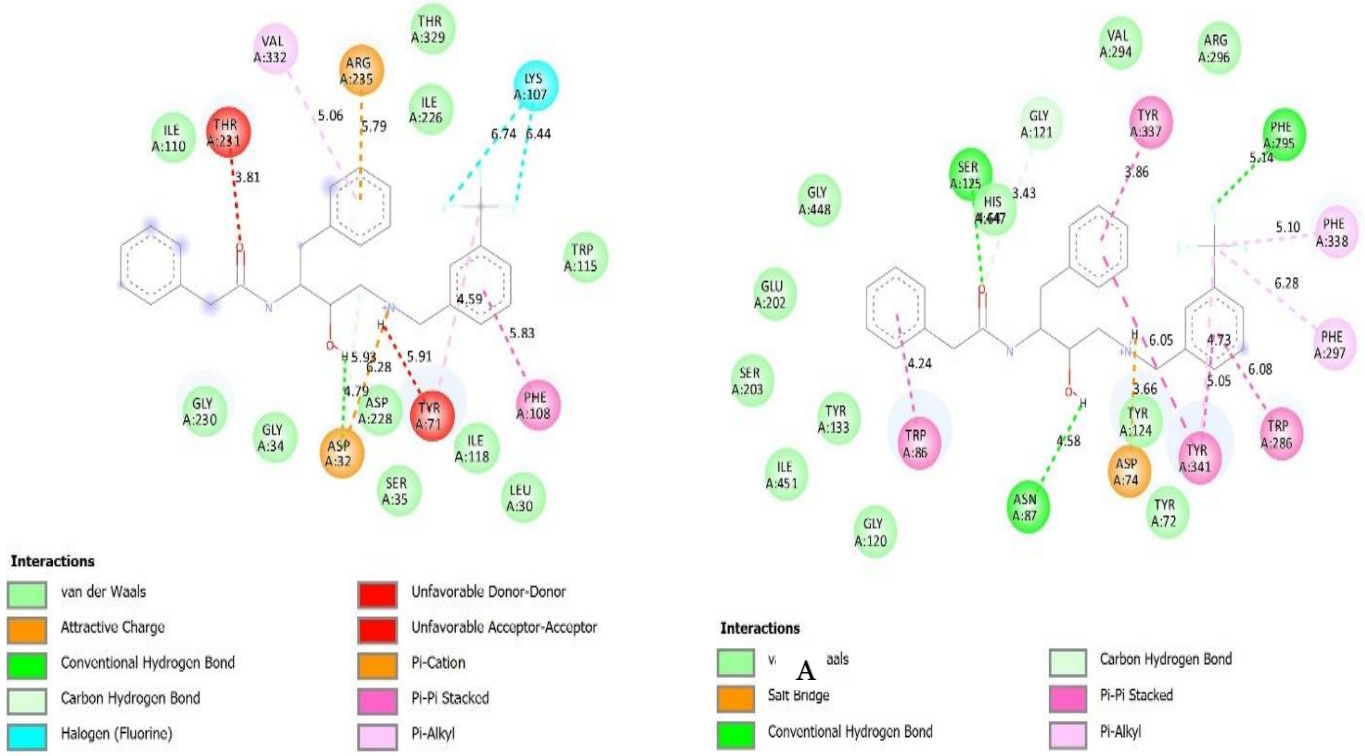
It was also shown that all the designed analogs were predicted to be substrates of CYP3A4 and CYP2D6. Inhibitory profiling indicated that every analog inhibits CYP3A4 and CYP2C19, while CYP1A2 inhibition is restricted to B7 and B9. Predicted total clearance values ranged from 0.801 Log ml/min/kg (B3) to 1.171 Log ml/min/kg (B9), with B5 (1.066), B8 (1.051), and B9 (1.171) cleared more rapidly than compound 10 (0.68 log ml/min/kg) which provides the extent of drug elimination from the body (Talevi & Bellera, 2021). None of the designed analogs or compound 10 were identified as substrates of renal organic cation transporter 2 (OCT2), which reduces the likelihood of OCT2-mediated renal toxicity or drug–drug interactions (Ugbe *et al*., 2023c). Also, most analogs were predicted to be non-mutagenic, with nine out of ten (all except B4) giving negative Ames test predictions. In terms of cardiotoxicity, only B10 was predicted to inhibit the hERG I potassium channel, whereas the remaining analogs showed no hERG I inhibition, indicating a low risk of drug-induced arrhythmia. No skin sensitization liability was observed across the series. With respect to hepatotoxicity, most compounds showed a potential hepatotoxic signal; however, B3, B10, and donepezil were predicted to be non-hepatotoxic. Based on the drug-likeness, ADME, and toxicological analyses conducted, the newly designed analogues showed good pharmacokinetic properties and were compared favourably with the lead compound and reference drug.

3.10. Target selectivity profile of the designed analogs

The wide-ranging therapeutic potential, binding specificity, and off-target safety of the designed hydroxyethylamine analogs were assessed by integrating multi-target docking (Table 5),

drug-likeness analysis (Table 6), and ADMET profiling (Table 7). The primary biological target, BACE1, was evaluated together with secondary neurological targets (AChE and the D2 dopamine receptor) and the off-target kinase FGFR3. The combined analysis of binding geometries, key active-site interactions, and pharmacokinetic parameters (HIA, LogBB, clearance, metabolic inhibition, and toxicity alerts) identified analogs B2 and B5 as the most balanced lead compounds.

In their interactions with BACE1, B2 forms conventional hydrogen bonds and charge-assisted electrostatic contacts with ASP32 (4.79 Å) and ASP228 (5.93 Å), closely mimicking the interaction pattern required for catalytic blockade (Figure 10A). Additional stabilization arises from halogen bonds between the trifluoromethyl group and LYS107 (6.44 Å and 6.74 Å), a π-cation interaction with ARG235 (5.79 Å), and hydrophobic contacts involving VAL332 and PHE108. In Figure 11A, B5 displays a similar binding orientation, anchoring directly to ASP228 via a hydrogen bond (4.85 Å) and forming a strong salt bridge with ASP32 (4.52 Å). The tetrahydrofuran oxygen further engages ARG235 through a hydrogen bond (5.03 Å), while THR231 (4.86 Å) stabilizes the ligand backbone. Halogen interactions with LYS107 (6.36 Å and 6.88 Å) and π-alkyl contacts with PHE108 (3.97 Å) and VAL332 (5.31 Å) help secure B5 within the BACE1 active cleft.



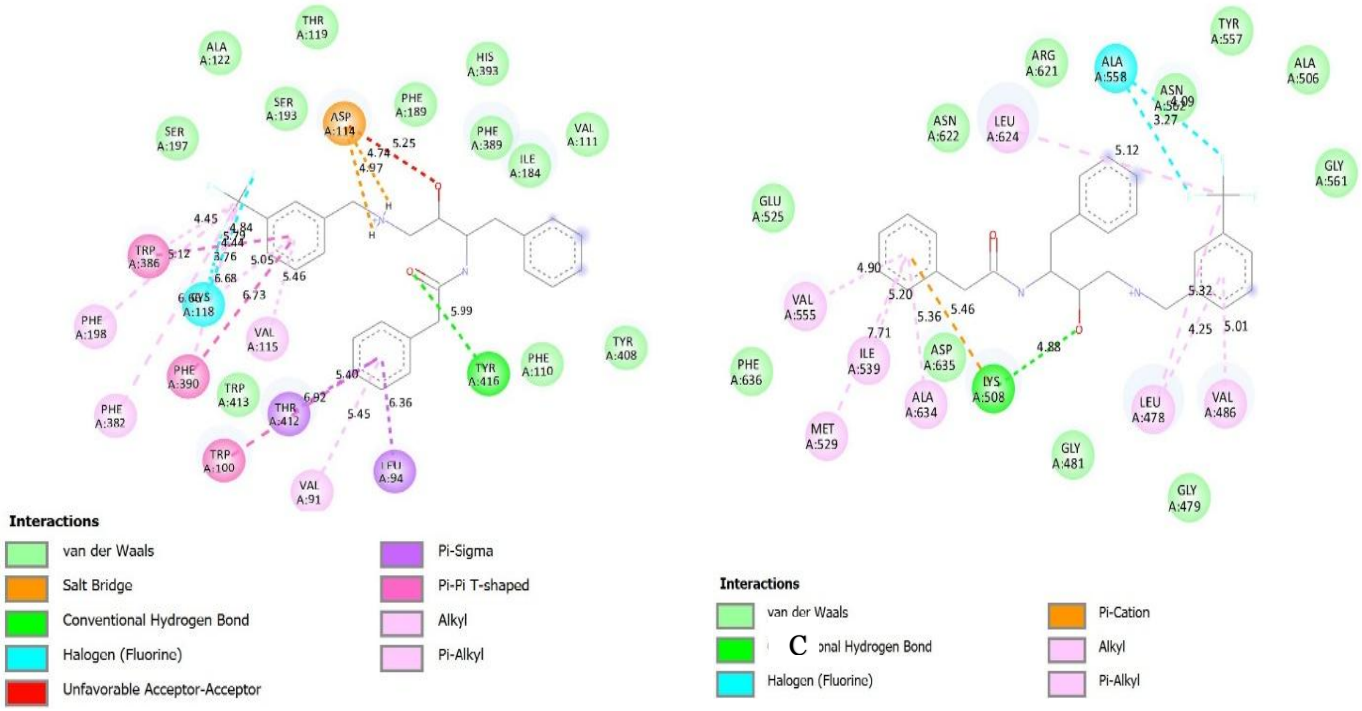


Figure 10. Docked poses of designed ligand B2 with (A) BACE1 (PDB ID: 2ZHV), (B) AChE (PDB ID: 4EYZ), (C) D2 Dopamine receptor (PDB ID: 6CM4), and (D) FGFR3 (PDB ID: 6LVM).

For off-target interactions with AChE, Figure 10B shows that B2 engages both the catalytic active site (CAS) and the peripheral anionic site (PAS). It forms double hydrogen bonds with SER125 (3.43 Å) and ASN87 (4.58 Å), a strong salt bridge with ASP74 (3.66 Å), and a halogen interaction with PHE295 (5.14 Å). Its aromatic rings participate in π–π stacking with PAS residues TRP86 (4.24 Å), TYR337 (3.86 Å), TYR341 (4.73 Å), and TRP286 (6.08 Å), supporting dual-site binding. As depicted in Figure 11B, B5 similarly shows dual engagement of CAS and PAS, forming hydrogen bonds with SER125 (4.48 Å) and TYR72 (4.95 Å), together with an attractive charge/salt-bridge interaction with ASP74 (5.16 Å). Aromatic stabilization is maintained through π–π contacts with TRP86 (5.00 Å), TYR124 (5.41 Å), and TRP286 (4.88 Å).

Cross-reactivity with the D2 dopamine receptor is illustrated in Figure 10C, where B2 forms an ionic salt bridge between its protonated amine and the orthosteric aspartate ASP114 (4.74 Å and 4.97 Å). Halogen interactions are established with CYS118 (3.76 Å), and an extended network of π–π T-shaped and π-alkyl contacts involving TRP386, PHE390, THR412, and VAL115 stabilizes the complex within the receptor pocket. Figure 11C shows that B5 also binds ASP114 via a salt bridge (4.92 Å) and forms multiple halogen contacts with CYS118 (3.64 Å and 4.43 Å). Hydrophobic and π-stacking interactions with TRP386 (5.09 Å), PHE390 (5.10 Å), THR412 (5.86 Å), and ILE184 (4.95 Å) further contribute to its binding, highlighting a similar D2 receptor engagement pattern to B2.

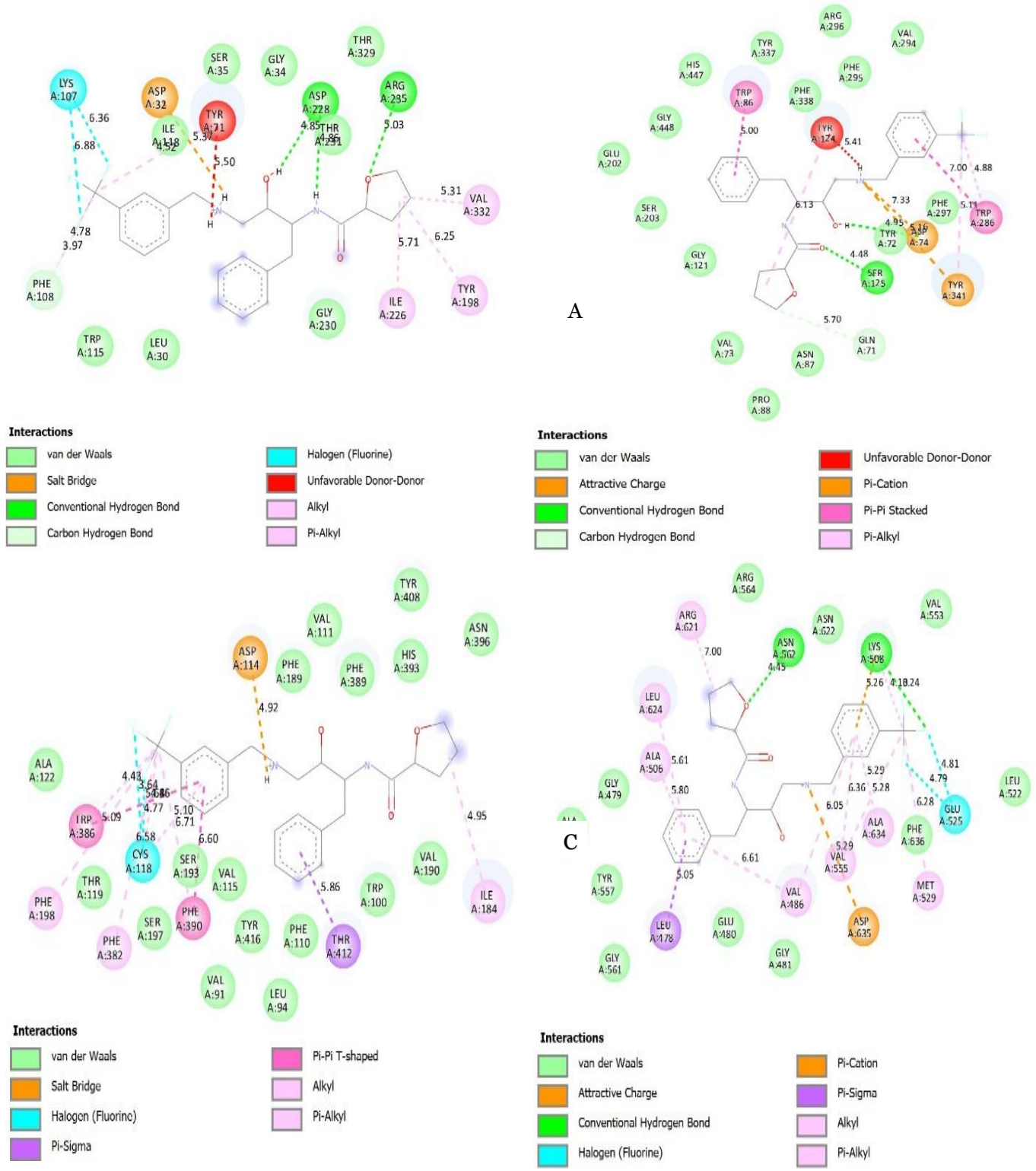


Figure 11. Docked poses of designed ligand B5 with (A) BACE1 (PDB ID: 2ZHV), (B) AChE (PDB ID: 4EYZ), (C) D2 Dopamine receptor (PDB ID: 6CM4), and (D) FGFR3 (PDB ID: 6LVM).

The interaction profile with FGFR3 (Figure 10D) indicates that B2 occupies the ATP-binding region, forming a hydrogen bond with LYS508 (4.88 Å) and halogen contacts with ALA558 and ASN562 (3.27 Å and 4.09 Å). Surrounding hydrophobic interactions with VAL555,

ILE539, MET529, ALA634, and LEU478 contribute to local stabilization, suggesting measurable but not dominant kinase engagement. In Figure 11D, B5 interacts with the hinge/ATP pocket through hydrogen bonds to ASN562 (4.45 Å) and LYS508 (4.10 Å and 4.24 Å), together with halogen contacts to GLU525 (4.79 Å and 4.81 Å). π-alkyl and π-cation interactions involving LYS508, ASP635, VAL555, LEU478, and LEU624 further support binding.

Consequently, both B2 and B5 fully comply with Lipinski's Rule of Five and exhibit superior aqueous solubility (LogS = −5.11 and −4.19, respectively) compared with the poorly soluble template compound 10 (LogS = −6.63). Their synthetic accessibility (SA) scores (3.66 for B2 and 3.88 for B5) also indicate easier synthetic feasibility relative to the parent compound (4.15). In terms of CNS penetration and absorption, B2 achieves the highest predicted blood–brain barrier permeability in the series (LogBB = 0.129), exceeding both donepezil (0.048) and compound 10 (−0.012), making it a strong central nervous system candidate (Thai *et al*., 2020). B5 shows high human intestinal absorption (87.23%) and rapid total metabolic clearance (1.066 Log ml/min/kg), supporting favorable systemic handling. Importantly, both analogs are predicted to be non-mutagenic (Ames negative) and free of hERG I potassium channel inhibition alerts, indicating a low cardiotoxicity risk. In conclusion, based on this combined multi-target docking, drug-likeness, and ADMET evaluation, newly designed analogs B2 and B5 were selected as primary lead candidates for downstream molecular dynamics (MD) simulations to investigate their thermodynamic stability, conformational flexibility, and dynamic binding persistence in aqueous environments.

3.11 Molecular dynamics simulation

The structural stability, conformational flexibility, compactness, and intermolecular hydrogen-bonding networks of the complexes were evaluated. A 200 ns all-atom molecular dynamics (MD) simulations were performed for the reference inhibitor (donepezil), template ligand 10, and two selected leads (B2 and B5). Time-dependent trajectories and average MD parameters are summarized in Figures 12 (a–e) and Table 8.

Table 8

Average values of RMSD, RMSF, RoG, SASA, and number of hydrogen bonds for Donepezil, Template ligand 10, and lead compounds B2 and B5 over 200 ns MD simulations.

Molecule	Parameters				
	RMSD (Å)	RoG (Å)	RMSF (Å)	SASA ($Å^2$)	H-Bond
Donepezil	3.75	29.27	1.96	27,084.66	52.24
B2	2.99	28.88	1.51	24,559.99	57.42
B5	4.16	29.44	2.09	26,544.73	53.21
Template L. 10	4.36	29.19	2.08	25,907.57	54.81

The root mean square deviation (RMSD) of the protein backbone atoms was monitored over the 200 ns simulation to assess complex equilibration (Figure 12a). As shown in Table 8, compound B2 exhibited the lowest average RMSD value (2.99 Å). Donepezil, B5, and template ligand 10 displayed noticeable trajectory drift between 80 and 180 ns (peaking between 5.0 and 7.0 Å), whereas B2 attained a steadily equilibrated trajectory after ~100 ns, plateauing near 3.5–4.0 Å. This pronounced structural stabilization indicates that B2 induces minimal conformational perturbation within the binding pocket compared with the parent template and standard drug. Local residue mobility was assessed through root mean square fluctuation (RMSF) calculations (Figure 12b). Consistent with the RMSD trends, the B2 complex demonstrated the lowest mean global flexibility (1.51 Å), compared with donepezil (1.96 Å), B5 (2.09 Å), and template ligand 10 (2.08 Å). Significant fluctuations (RMSF > 3.0 Å) observed in flexible loop regions around residues 200–240 and 300–320 in the donepezil and template ligand 10 complexes were substantially suppressed upon B2 binding. This localized damping highlights strong active-site contacts, anchoring key pocket residues and enhancing active-site rigidity.

The overall protein compactness and hydrophobic core integrity were evaluated using the radius of gyration (RoG, Figure 12c) and solvent-accessible surface area (SASA, Figure 12d). B2 yielded the most compact complex architecture, with an average RoG of 28.88 Å and the lowest mean SASA value (24,560 Å^2). The sustained reduction in SASA for B2 relative to donepezil (27,085 Å^2) suggests more extensive hydrophobic burial of the lead scaffold within the binding site, limiting solvent exposure and helping to preserve the tertiary fold throughout the simulation. Hydrogen-bond formation dynamics were tracked over the 200 ns simulation to evaluate binding tenacity (Figure 12e). Compound B2 maintained a dense network of noncovalent interactions, with an average of 57.42 hydrogen bonds over the simulation. In comparison, donepezil, B5, and template ligand 10 formed average counts of 52.24, 53.21, and 54.81, respectively. The higher occupancy and density of hydrogen bonds in the B2 complex provide a structural rationale for its enhanced thermodynamic binding affinity.

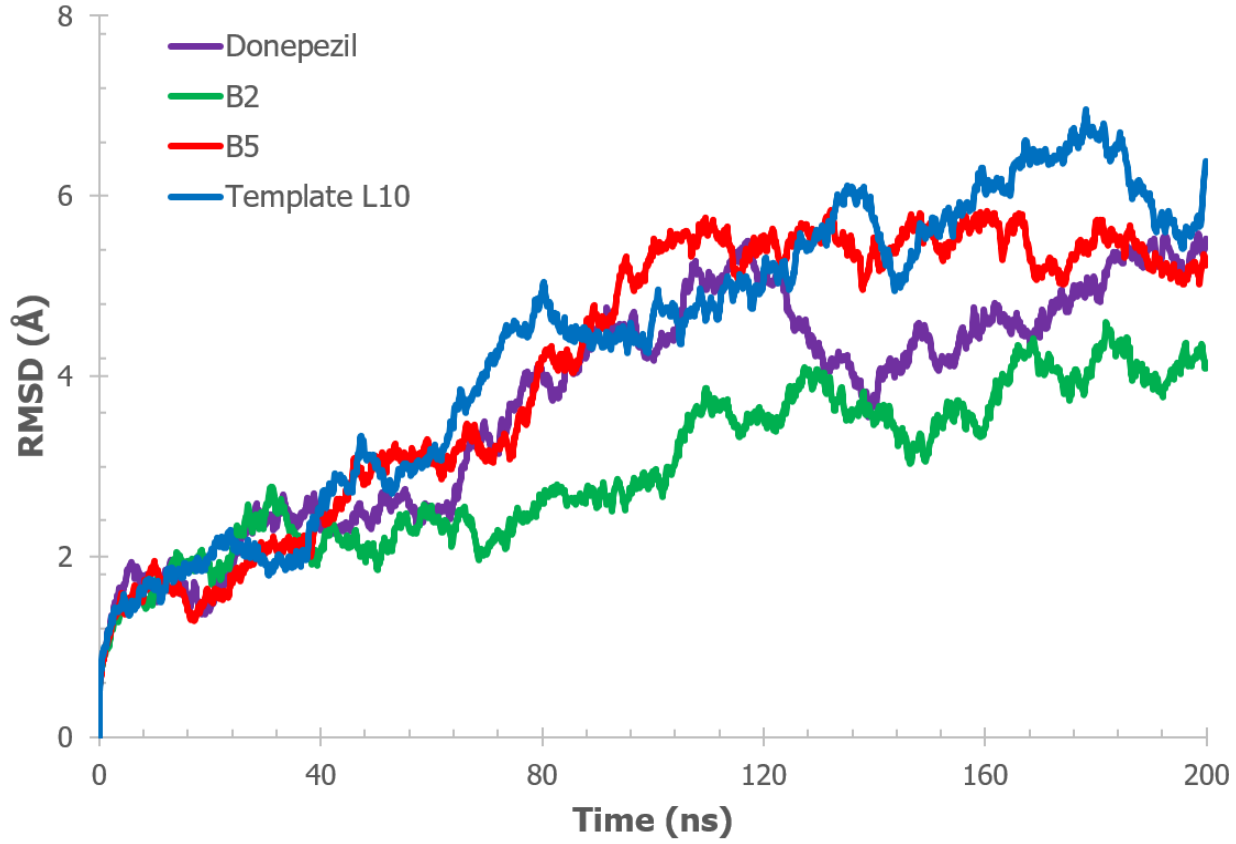


Figure 12a. RMSD

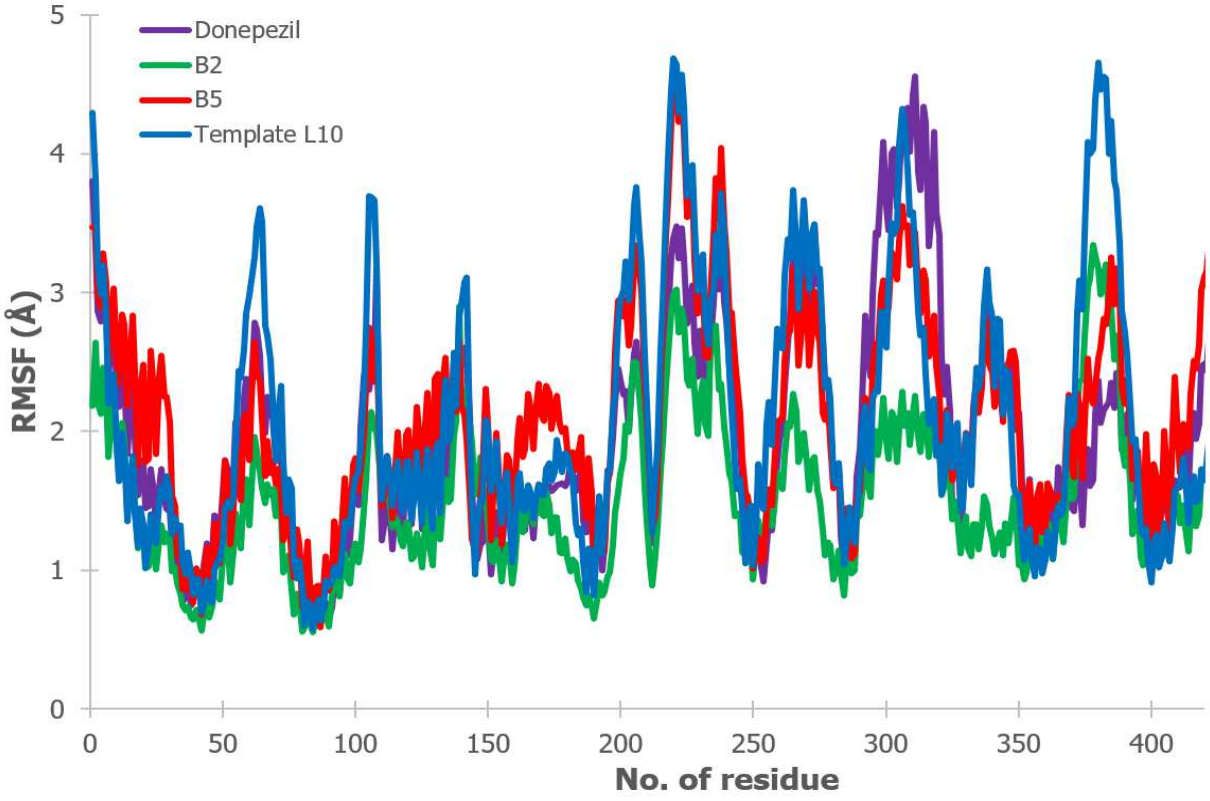


Figure 12b. RMSF

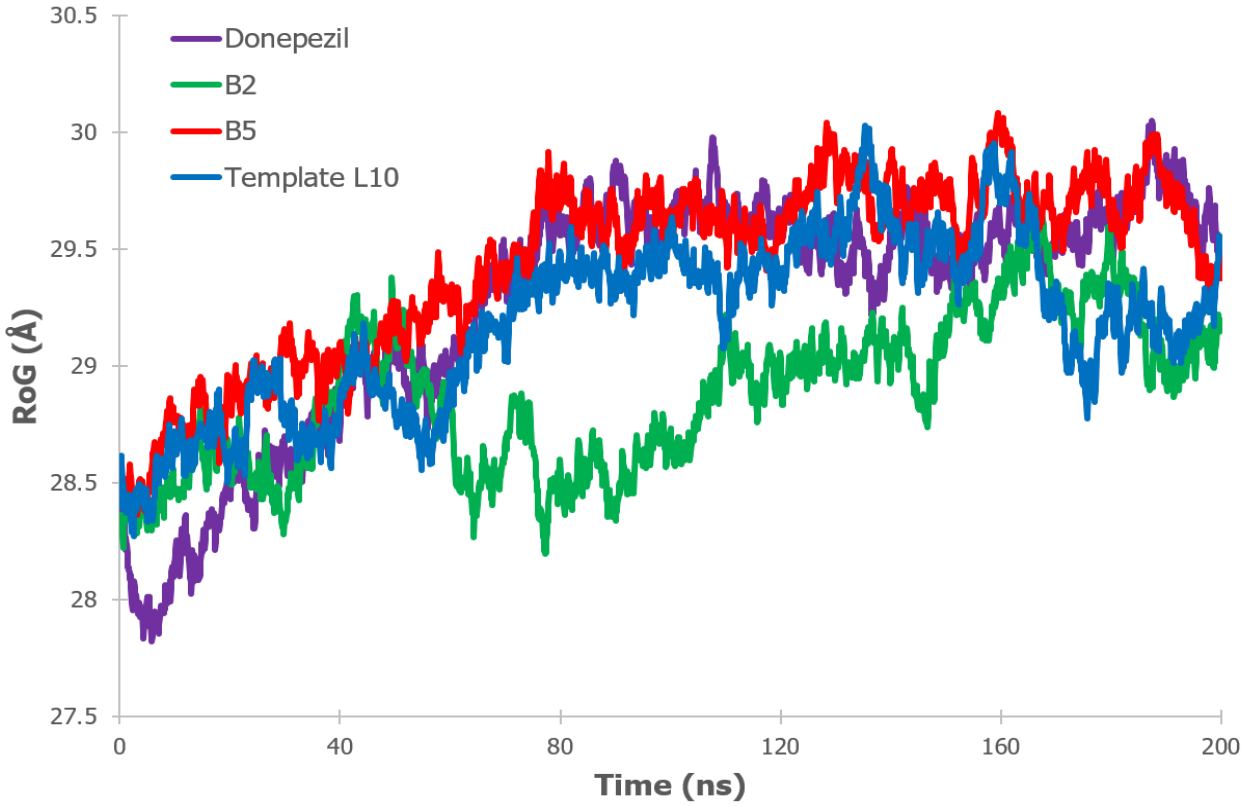


Figure 12c. RoG

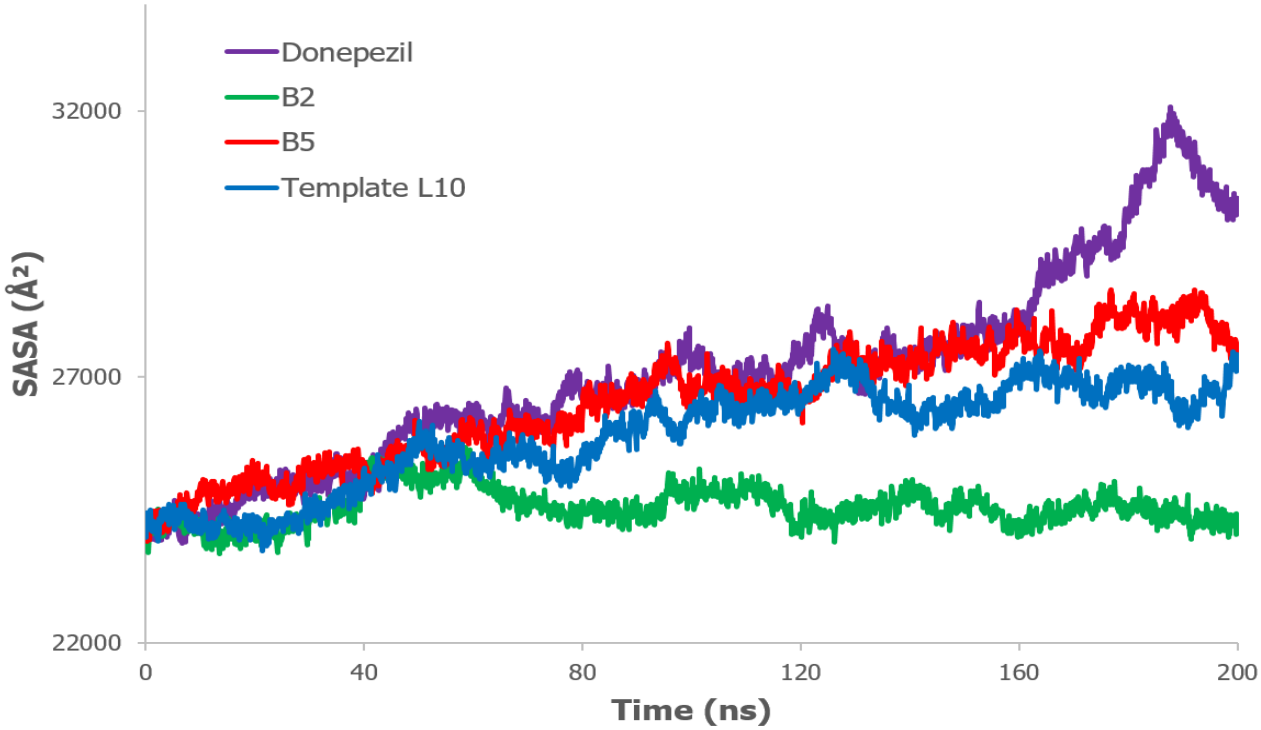


Figure 12d. SASA

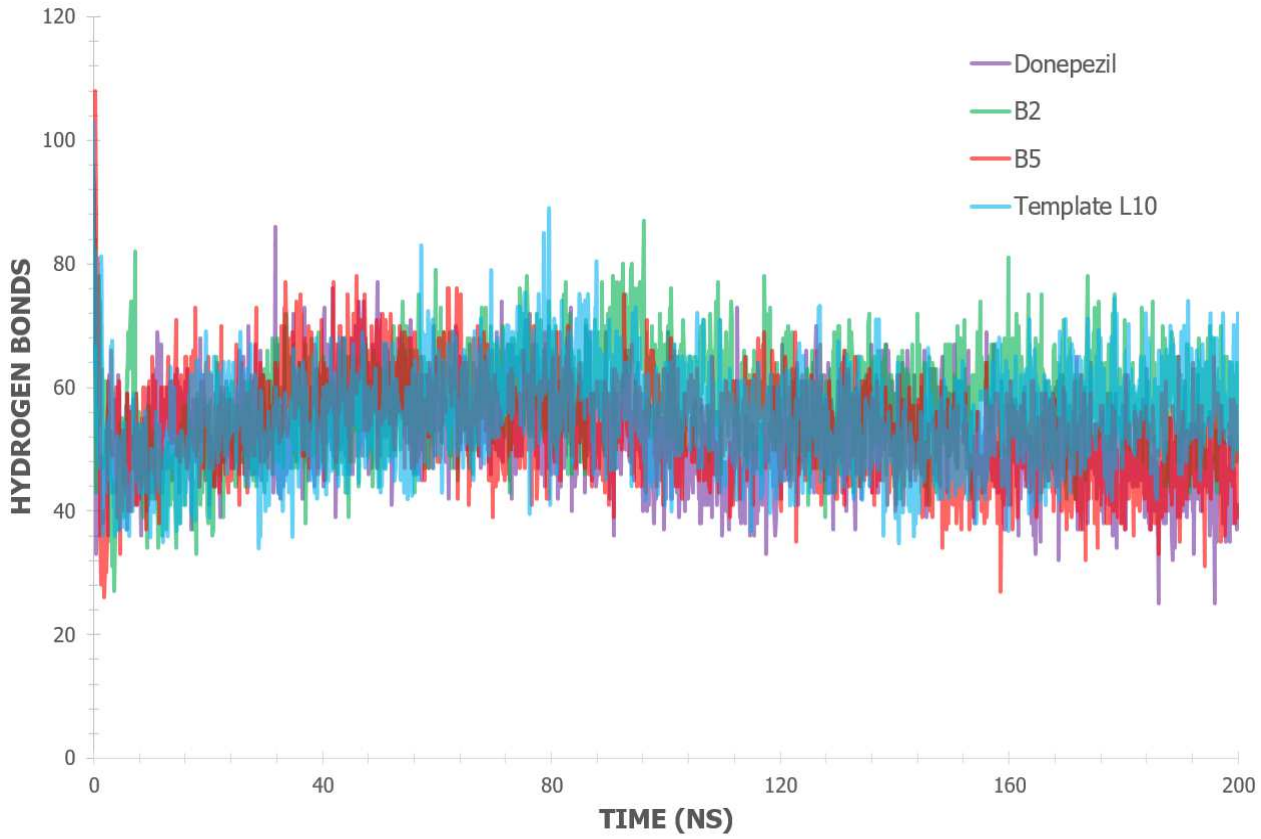


Figure 12e. H-Bond

Figure 12. Molecular dynamics (MD) simulation results for 200 ns trajectories of the Alzheimer's inhibitor complexes: (A) RMSD, (B) RoG, (C) RMSF, (D) SASA, and (E) number of hydrogen bonds.

3.12 Binding affinity and free energy analysis

Thermodynamic binding profiles and noncovalent forces stabilizing the complexes, end-point binding free energy calculations comprising LIE, MM/PBSA, and MM/GBSA were performed over the equilibrated simulation trajectories (Tables 9–11).

Table 9

Linear interaction energy (LIE) calculation of the complexes.

Name	Van der Waals (kcal/mol)	Electrostatic (kcal/mol)	**Total LIE** (kcal/mol)
Donepezil	-51.3133	-12.8758	**-13.4854**
B2	-53.7183	-37.6228	**-22.0848**
B5	-49.9822	-36.5678	**-21.0642**
Template ligand 10	-53.4749	-50.1754	**-26.1834**

The LIE method estimates binding affinity by evaluating the differences in nonbonded van der Waals and electrostatic interaction energies between the solvent-bound and receptor-bound states (Table 9). All designed compounds and the template exhibited substantially more favorable binding than the reference drug donepezil (−13.49 kcal/mol). Template ligand 10 showed the most favorable LIE binding energy (−26.18 kcal/mol), followed by lead candidate B2 (−22.08 kcal/mol) and B5 (−21.06 kcal/mol). Nonpolar van der Waals interactions were the dominant driving force for all ligands, contributing between −49.98 and −53.72 kcal/mol. MM/PBSA calculations yielded binding free energies consistent with the LIE trends, with template ligand 10 and lead B2 displaying more favorable ΔG_{bind} values than donepezil (Table 10).

Table 10

MM/PBSA calculation for the complexes.

Parameters	Donepezil (Mean/SD)	B2 (Mean/SD)	B5 (Mean/SD)	Template ligand 10 (Mean/SD)
Electrostatic	-12.8758/5.1217	-37.8816/6.4929	-36.5679/5.2734	-50.1754/5.8089
Van der Waals	-51.3133/2.5824	-53.6642/3.4544	-49.9822/3.0560	-53.4749/3.0933
Poisson-Boltznann	63.8405/6.5998	79.7468/5.9292	81.3571/4.8897	87.6921/5.4277
Solvent Accessible	-6.0203/0.0972	-6.6310/0.1341	-6.4616/0.1080	-7.3294/0.1170
Gas Phase Energy	-64.1891/5.2336	-91.5458/5.9415	-86.5500/4.9942	-103.6503/5.5361
Solvation Energy	57.8202/6.6169	73.1158/5.9415	74.8955/4.8606	80.3627/5.4022
Polar Contribution	50.9647/4.4094	41.8652/4.7989	44.7893/4.8131	37.5167/4.5551
Non-polar Contribution	-57.3336/2.5944	-60.2952/3.4886	-56.4438/3.0701	-60.8043/3.1209
Total Energy	**-6.3689/4.0609**	**-18.4300/3.9237**	**-11.6545/4.4511**	**-23.2876/4.0757**

The implicit Generalized Born solvation model produced consistent energetic trends across all systems. Both designed leads, B2 (−51.45 kcal/mol) and B5 (−50.64 kcal/mol), together with template ligand L10 (−55.21 kcal/mol), exhibited markedly more favorable binding free energies than the reference drug donepezil (−38.67 kcal/mol) (Table 11). Van der Waals packing (ΔE_{vdW}) was the primary thermodynamic driver for all four complexes, ranging from −50.92 to −58.11 kcal/mol. B2 displayed an exceptionally favorable net polar contribution ($\Delta E_{elec}+\Delta G_{solv}$= +0.03 kcal/mol), indicating that its electrostatic interaction network effectively compensates for the polar desolvation penalty. This thermodynamic efficiency enables B2 to achieve a binding affinity comparable to that of template ligand 10 while maintaining favorable trajectory stability.

Table 11:

MM/GBSA calculation for the complexes.

Names	△E(internal)	△E(electrostatic)+ △G(sol)	△E(VDW)	**△G binding** (kcal/mol)
Donepezil	-0	12.2514	-50.9213	**-38.6699 +/- 0.0739**
B2	0	0.0345	-51.4885	**-51.454 +/- 0.0814**
B5	-0	3.4707	-54.1089	**-50.6382 +/- 3.286**
Template ligand 10	-0	2.9033	-58.1144	**-55.2111 +/- 0.1002**

All three end-point binding free energy methods (LIE, MM/PBSA, and MM/GBSA) yielded a consistent relative ranking: template ligand 10 exhibited the highest binding affinity, lead B2 emerged as the top newly designed candidate (closely followed by B5), and donepezil consistently displayed the weakest binding energy.

3.13 Hydrogen bond dynamics and occupancy analysis

The directional electrostatic stability and persistence of ligand–receptor contacts over the 200 ns production phase was evaluated by examining key hydrogen-bond occupancies (cutoff > 2.0%) together with time-resolved H-bond frequency profiles (Table S3, Figure S1). B2 stood out for its exceptionally strong hydrogen-bonding pattern. Its dominant interaction involved the ligand side chain and ASP114, with an occupancy of 118.60%. Values above 100% arise when a single donor forms a bifurcated hydrogen bond, simultaneously engaging both carboxylate oxygens of ASP114 throughout the trajectory. Additional, weaker side-chain contacts were detected with PHE390 (4.25%) and CYS118 (2.75%). Template ligand 10 displayed the most extensive hydrogen-bonding network, with seven distinct interactions exceeding the 2.0% threshold. The complex was primarily anchored by ASP114 (78.55% occupancy), supported by secondary contacts to TYR416 (4.60% and 2.70%), CYS118 (3.80%), PHE390 (3.60%), TRP386 (2.65%), and PHE198 (2.20%). B5 preserved the critical catalytic anchor at ASP114, albeit at a more moderate occupancy of 23.30%, and formed additional interactions with CYS118 (8.75%) and THR412 (2.70%). In contrast, donepezil did not establish a strong, primary catalytic anchor. Its hydrogen bonds were distributed more weakly across TRP386 (19.85% backbone–side chain; 2.70% side chain–side chain), THR412 (15.70%), and VAL111 (6.50% side chain; 2.50% backbone). Time-series plots of H-bond counts across all 2,000 trajectory frames reinforced these stability trends (Figure S1). B2 maintained a dense profile, fluctuating continuously between 1 and 3 concurrent hydrogen bonds, with occasional peaks reaching 3.5–4.0 bonds. Template ligand 10 showed a similarly high-density pattern, mostly oscillating between 1 and 3 bonds and briefly attaining up to 5 simultaneous bonds. Donepezil and B5, by contrast, exhibited sparser profiles, typically fluctuating between 0 and 1 bond over time. The persistent, bifurcated engagement of ASP114 by B2 aligns directly with its highly favorable electrostatic interaction energy (ΔE_{elec} = −37.88 kcal/mol), offering a clear structural explanation for its superior binding affinity relative to donepezil.

3.14 Principal component analysis

Principal component analysis (PCA) was employed to probe the global conformational dynamics and phase-space behavior of the protein–ligand complexes. Trajectory frames were projected onto the two-dimensional essential subspace spanned by the first two principal components (PC1 vs PC2) (Table S2). For all four complexes (see Supplementary Information), the leading eigenvectors (PC1 and PC2) together account for more than 75% of the total collective atomic fluctuations. This confirms that the reduced 2D projection captures the dominant macro-domain motions that govern system stability. B5 shows the strongest variance concentration along PC1 (78.09%), consistent with a highly directional global conformational transition toward a single thermodynamic minimum. By contrast, B2 displays a more distributed variance pattern (57.18% along PC1 and 18.73% along PC2), pointing to greater multi-directional domain mobility. Two-dimensional projections onto PC1 and PC2 were plotted in a common coordinate space (Figure S2a–d). B2 samples a broad conformational landscape, with PC1 ranging from −70 to +55 and PC2 from −30 to +60. Although it visits multiple intermediate basins during the middle portion of the trajectory (teal/green frames), it ultimately collapses into a localized equilibrium cluster around PC1 ≈ −50, PC2 ≈ 0, and indicating convergence toward a stable conformational substate. The tight clustering of terminal frames for B5, template ligand L10, and donepezil confirms that these ligands stabilize compact, well-defined conformational states in the target protein, suppressing unbinding events and large-scale destabilizing fluctuations

4. Conclusion

This research work delivers a statistically robust five-descriptor GA-MLR QSAR model that links the molecular design of hydroxyethylamine (HEA) derivatives to their multi-target inhibitory potential. Internal cross-validation ($Q^2LOO = 0.7965$), external prediction ($Q^2F3 = 0.6995$), Y-scrambling tests, and leverage-based applicability-domain analysis together confirm that the model is reliable and predictive within a well-defined chemical space. The selected descriptors highlight specific electronic, steric, and structural features that govern activity, providing concrete handles for further lead optimization. Multi-target docking against BACE1, AChE, the D2 dopamine receptor, and FGFR3 shows that the newly designed derivatives, particularly leads B2 and B5, occupy catalytic and binding pockets across all four targets with high thermodynamic favorability. Their predicted binding affinities range from 6.77 to 11.50 kcal/mol, outperforming both the template parent molecule and reference drugs (donepezil, galantamine, and rivastigmine). In silico ADMET and pharmacokinetic assessments indicate that B2 and B5 comply with Lipinski's rule of five, display favorable central nervous system exposure, and achieve acceptable blood–brain barrier permeability (log BB = 0.129 for B2 and 0.975 for B5), with no red

flags for mutagenicity or hERG channel inhibition. The 200 ns all-atom molecular dynamics simulations and associated trajectory analyses (RMSD = 2.99 Å, together with RMSF, radius of gyration, SASA, and hydrogen-bonding networks) confirm that B2 and B5 form stable, compact, and persistent macromolecular complexes. Independent end-point binding free-energy calculations using LIE, MM/PBSA, and MM/GBSA (ΔGbind = −51.45 kcal/mol for B2 and −50.64 kcal/mol for B5) reinforce the thermodynamic drivers and noncovalent interactions that stabilize these complexes. In view of the foregoing, these results position hydroxyethylamine-based MTDLs, particularly B2 and B5, as multi-functional scaffolds worthy of experimental pursuit. Recommended next steps are to use B2 and B5 as core templates for wet-lab synthesis, in vitro enzymatic assays against BACE1, AChE, D2, and FGFR3, and further 3D-QSAR/pharmacophore-guided refinement toward practical therapeutic leads for Alzheimer's disease.

Funding

This research received no external funding.

CRediT authorship contribution statement

Muhammad Abubakar Dagoli: Conceptualization, data curation, formal analysis, funding acquisition, investigation, methodology, project administration, resources, software, validation, visualization, writing – original draft, writing – review and editing. **Ahmed Umar:** Conceptualization, data curation, funding acquisition, project administration, resources, supervision, validation, visualization, writing – original draft, writing – review and editing. **Fabian Audu Ugbe:** Conceptualization, formal analysis, funding acquisition, methodology, project administration, resources, software, supervision, validation, visualization, writing – original draft, writing – review and editing. **Emmanuel Israel Edache:** Methodology, project administration, software, validation, visualization, writing – original draft, writing – review and editing.

Declaration of competing interests

The authors declare that they have no known competing financial interests or personal relationships that could have appeared to influence the work reported in this paper.

Ethics approval and consent to participate: Not applicable.

Consent for publication: Not applicable.

Clinical trial registration: Not applicable (this study does not involve human subjects or clinical trials).

Acknowledgements

The authors express their sincere gratitude to Mr. Baju Festus Akapson (Department of Chemistry, Faculty of Science, University of Abuja, Old Campus, Gwagwalada, Abuja, Nigeria) for his invaluable technical support and guidance throughout this study.

Supplementary materials

Supplementary data associated with this article are available in the online version of the manuscript.

Data availability

The data supporting the findings of this study are available from the corresponding author upon request.

References

Abdullahi A, Shallangwa G.A, Ibrahim M.T, Bello A.U, Arthur D.E, Uzairu A, Mamza P., 2019. QSAR studies on some C14-urea tetrandrine compounds as potent anti-cancer agents against Leukemia cell line (K562). JOTCSA 5 (3):1391–1402.

Adeniji S.E, Uba S, Uzairu A., 2019. Activity modeling of some potent inhibitors against mycobacterium tuberculosis using genetic function approximation approach. Adıyaman Univ J Sci 9(1):77–98.

Adeniji SE, Uba S, Uzairu A., 2018. QSAR modeling and molecular docking analysis of some active compounds against mycobacterium tuberculosis receptor (Mtb CYP121). J Path Hindawi 2018:24–64.

Arthur, D.E., Soliman, M. E.S., Adeniji, S. E., Adedirin, O., Peter, F., 2022. QSAR and molecular docking study of gonadotropin-releasing hormone receptor inhibitors, Scientific African, 17, e01291, 2468-2276. https://doi.org/10.1016/j.sciaf.2022.e01291.

Arthur, D.E., Uzairu, A., Mamza, P., Abechi, S.E., Shallangwa, G.A., 2018. Activity and Toxicity Modelling of Some NCI Selected Compounds against Leukemia P388adr Cell Line Using Genetic Algorithm-Multiple Linear Regressions, Journal of King Saud University-Science.

Azmal M, Paul JK, Shohan MNH, Haque ANMSNB, Mrinmoy M, Talukder OF, Ghosh A., 2025. Evaluating computational and experimental approaches in early-stage Alzheimer's drug discovery: a systematic review. J. Comput. Aided Mol. Des., 39 (1):27. https://doi.org/10.1007/s10822-025-00610-7.

Bai, Q., Tan, S., Xu, T., Liu, H., Huang, B., Yao, X., 2021. MolAICal: A soft tool for 3D drug design of protein targets by artificial intelligence and classical algorithms, Brief. Bioinform. 22 (3) bbaa161. https://doi.org/10.1093/bib/bbaa161.

Bajda M, Guzior N, Ignasik M, Malawska B., 2011. Multi-target-directed ligands in Alzheimer's disease treatment. Curr Med Chem. (2011) 18 (32):4949-75. https://doi.org/10.2174/092986711797535245.

Bazzari, F.H., Bazzari, A.H., 2022. BACE1 inhibition for Alzheimer's disease: the past, present and any future, Molecules, 27 (24) 8823. https://doi.org/10.3390/molecules27248823.

Bocharov, E.V., Lesovoy, D.M., Goncharuk, S.A., Goncharuk, M.V., Hristova, K., Arseniev, A.S., 2013. Structure of FGFR3 transmembrane domain dimer: implications for signaling and human pathologies. Structure. 21 (11) 2087-93. https://doi.org/10.1016/j.str.2013.08.026.

Bozkır İ, İbişoğlu M.S, Kayıkçıoğlu Bozkır İ, Güler H.İ., 2026. Computational prioritization of multi-target inhibitors: explainable QSAR and docking-based discovery of dual AChE/BACE1 chemotypes. J. Comput Aided Mol Des., 40 (1):54. https://doi.org/10.1007/s10822-025-00757-3.

Chen, Z.R., Huang, J.B., Yang, S.L., Hong, F.F., 2022. Role of cholinergic signaling in Alzheimer's disease, Molecules. 27 1816. https://doi.org/10.3390/molecules27061816.

Chirico, A., Todeschini, V., 2017. Beware of unreliable Q^2! A comparative study of regression metrics for predictivity assessment of QSAR models, *J. Chem. Inf. Model.* 57, 318–332. https://doi.org/10.1021/acs.jcim.6b00277.

Daina, A., Michielin, O., Zoete, V., 2017. SwissADME: a free web tool to evaluate pharmacokinetics, drug-likeness, and medicinal chemistry friendliness of small molecules, Sci. Rep. 7 42717. https://doi.org/10.1038/srep42717.

Daniel F. V., Stephen R. J., Hung-Yuan C., Brian R. S., Keith W. W., Kenneth D. K., 2002. *Journal of Medicinal Chemistry*, *45* (12), 2615-2623. https://doi.org/10.1021/jm020017n.

Eberhardt J, Santos-Martins D, Tillack A.F, Forli S., 2021. AutoDock Vina 1.2.0: New docking methods, expanded force field, and python bindings. Journal of Chemical Information and Modeling, 61 (8):3891–8.

Edache, E.I., Ugbe, F.A., Dawi, H.A., Adedayo, A., Umar, A., 2025. Mechanism of action of substituted peramivir phosphonate derivatives as potent oseltamivir-resistant influenza A virus using molecular docking, molecular dynamics simulations, and free energies calculations, Discov. Chem. 2 (1) 99. https://doi.org/10.1007/s44371-025-00184-1.

Edache, E.I., Uzairu, A., Abechi, S.E., 2015. Quantitative structure and activity relationship modeling study of anti-HIV-1 RT inhibitors: genetic function approximation and density function theory methods, J. Comput. Methods Mol. Des., 5 (4) 61–76.

Edache, E.I., Uzairu, A., Mamza, P.A., Shallangwa, G.A, Ibrahim, M.T., 2024. Evaluation of novel Anti-SARS-CoV-2 compounds by targeting nucleoprotein and envelope protein through homology modeling, docking simulations, ADMET, and molecular dynamic simulations with the MM/GBSA calculation, Intell. Pharm., 2 (3) 346–366. https://doi.org/10.1016/j.ipha.2024.02.008.

Edache, E.I., Uzairu, A., Mamza, P.A., Shallangwa, G.A, Ibrahim, M.T., 2024b. Design of some potent non-toxic Autoimmune disorder inhibitors based on 2D-QSAR, CoMFA, molecular docking, and molecular dynamics investigations, Intelligent Pharmacy, 2 (5), 688-706. https://doi.org/10.1016/j.ipha.2023.12.009.

Gheidari, D., Mehrdad, M., & Karimelahi, Z., 2024. Virtual screening, ADMET prediction, molecular docking, and dynamic simulation studies of natural products as BACE1 inhibitors for the management of Alzheimer's disease. *Sci Rep* 14, 26431. https://doi.org/10.1038/s41598-024-75292-6.

Gramatica, P., 2007. Principles of QSAR Models Validation: Internal and External, Molecular Informatics 26 (5) 694–701.

Gramatica, P., 2014. External Evaluation of QSAR Models, in Addition to Cross-Validation: Verification of Predictive Capability on Totally New Chemicals. Mol. Inf., 33: 311-314. https://doi.org/10.1002/minf.201400030

Gramatica, P., Chirico, N., Papa, E., Cassani, S., Kovarich, S., 2013. QSARINS: A New Software for the Development, Analysis, and Validation of QSAR MLR Models, Journal of Computational Chemistry 34 (24) 2121–2132. https://doi.org/10.1002/jcc.23361.

Guerguer FZ, Khedraoui M, Samadi A, Chtita S., 2025. Computational Approaches for Multitarget Drug Design in Alzheimer's Disease: A Comprehensive Review. Curr Med Chem., 32 (32):7017-7044. https://doi.org/10.2174/0109298673320300240930064551.

Hanwell M.D, Curtis D.E, Lonie D.C, Vandermeersch T, Zurek E, Hutchison G.R., 2012. Avogadro: an advanced semantic chemical editor, visualization, and analysis platform. J Cheminf. 4 (1):17. https://doi.org/10.1186/1758-2946-4-17.

Hossain M.S, Hussain M.H., 2025. Multi-Target Drug Design in Alzheimer's Disease Treatment: Emerging Technologies, Advantages, Challenges, and Limitations. Pharmacol Res Perspect., 13 (4):e70131. https://doi.org/10.1002/prp2.70131.

Hussain, R., Ullah, H., Rahim, F., Sarfraz, M., Taha, M., Iqbal, R., Rehman, W., Khan, S., Shah, S.A.A., Hyder, S., Majid, A., Abdulhakeem, S.A., Osama, A., Mahmoud, A.A., 2022. Multipotent cholinesterase inhibitors for the treatment of Alzheimer's disease: Synthesis, biological analysis and molecular docking study of benzimidazole-based thiazole derivatives, Molecules. 27 6087. https://doi.org/10.3390/molecules27186087.

Jiansong Fang, Yongjie Li, Rui Liu, Xiaocong Pang, Chao Li, Ranyao Yang, Yangyang He, Wenwen Lian, Ai-Lin Liu, and Guan-Hua Du, 2025. Discovery of Multitarget-Directed Ligands against Alzheimer's Disease through Systematic Prediction of Chemical–Protein Interactions, Journal of Chemical Information and Modeling, 55 (1), 149-164, https://doi.org/10.1021/ci500574n.

Kabier M, Gambacorta N, Trisciuzzi D, Kumar S, Nicolotti O, Mathew B., 2024. MzDOCK: A free ready-to-use GUI-based pipeline for molecular docking simulations. Journal of Computational Chemistry 45(23):1980–6.

Kim D.K, Suh K, Park J, Lee S.E, Han J, Chang S, Kim Y, Mook-Jung I., 2024. FGFR3 drives Aβ-induced tau uptake. Exp Mol Med. 56 (7):1631-1642. https://doi.org/10.1038/s12276-024-01274-3.

Lipinski, C.A., 2002. Poor aqueous solubility – an industry wide problem in drug discovery, Am. Pharmaceut. Rev. 5 (3) 82–85.

Lipinski, C. A., Lombardo, F., Dominy, B. W., & Feeney, P. J., 2001. Experimental and computational approaches to estimate solubility and permeability in drug discovery and development settings. *Advanced Drug Delivery Reviews*, *46*(1-3), 3–26. https://doi.org/10.1016/s0169-409x(00)00129-0.

Liu, H., Hou, T., 2016. CaFE: A tool for binding affinity prediction using end-point free energy methods, Bioinformatics. 32 (14) 2216–2218. https://doi.org/10.1093/bioinformatics/btw215.

Neumann, U., 2011. Structure-based design, synthesis, and SAR of cyclic hydroxyethylamine (HEA) BACE-1 inhibitors. Bioorganic & Medicinal Chemistry Letters. https://doi.org/10.1016/J.BMCL.2011.02.038

Papa, E., Dearden, J., Gramatica, P., 2007. Linear QSAR Regression Models for the Prediction of Bioconcentration Factors by Physicochemical Properties and Structural Theoretical Molecular Descriptors, Chemosphere, 67 (2) 351–358.

Pasieka A, Panek D, Jończyk J, Godyń J, Szałaj N, Latacz G, Tabor J, Mezeiova E, Chantegreil F, Dias J, Knez D, Lu J, Pi R, Korabecny J, Brazzolotto X, Gobec S, Höfner G, Wanner K, Więckowska A, Malawska B., 2021. Discovery of multifunctional anti-Alzheimer's agents with a unique mechanism of action including inhibition of the enzyme butyrylcholinesterase and γ-aminobutyric acid transporters. Eur J Med Chem. 218:113397. https://doi.org/10.1016/j.ejmech.2021.113397.

Peitzika S.C, Pontiki E., 2023. A Review on Recent Approaches on Molecular Docking Studies of Novel Compounds Targeting Acetylcholinesterase in Alzheimer's Disease. Molecules. 28 (3):1084. https://doi.org/10.3390/molecules28031084.

Ramsay, R.R., Popovic-Nikolic, M.R., Nikolic, K., Uliassi, E., Bolognesi, M.L., 2018. A perspective on multi-target drug discovery and design for complex diseases, Clin. Interp. Med. Chem. 33 (4) 461–473. https://doi.org/10.1186/s40169-017-0181-2.

Talevi, A., Bellera, C.L., 2021. Total Clearance and Organ Clearance. In: The ADME Encyclopedia. Springer, Cham. https://doi.org/10.1007/978-3-030-51519-5_74-1.

Thai, N. Q., Theodorakis, P. E., & Li, M. S., 2020. Fast estimation of the blood-brain barrier permeability by pulling a ligand through a lipid membrane. *Journal of Chemical Information and Modeling*, *60*(6), 3057–3067. https://doi.org/10.1021/acs.jcim.9b00834.

Todeschini, R., Ballabio, D., Grisoni, F., 2016. *Journal of Chemical Information and Modeling* 2016 *56* (10), 1905-1913 https://doi.org/10.1021/acs.jcim.6b00277

Todeschini, R. and Consonni, V., 2009. Front Matter. In Molecular Descriptors for Chemoinformatics (eds R. Mannhold, H. Kubinyi, G. Folkers, R. Todeschini and V. Consonni). https://doi.org/10.1002/9783527628766.fmatter1.

Ugbe, F.A., Shallangwa, G.A., Uzairu, A., Abdulkadir, I., 2022a. Molecular docking-based virtual screening, molecular dynamic simulation, and 3-D QSAR modeling of some pyrazolopyrimidine analogs as potent anti-filarial agents, In Silico Pharmacol. 10 (1) 21. https://doi.org/10.1007/s40203-022-00136-y.

Ugbe, F.A., Edache, E.I., Adeniji, S.E., Arthur, D.E., Ajala, A., Adawara, S.N., Ibrahim, Z.Y.U., 2024. Computational evaluation of the inhibitory potential of some urea, thiourea, and selenourea derivatives of diselenides against leishmaniasis: 2D-QSAR, pharmacokinetics, molecular docking, and molecular dynamics simulation, J. Mol. Struct., 1302 137473. https://doi.org/10.1016/j.molstruc.2023.137473.

Ugbe, F.A., Shallangwa, G.A., Uzairu, A., Abdulkadir, I., 2023. Computational design, molecular properties, ADME, and toxicological analysis of substituted 2,6-diarylidene cyclohexanone analogs as potent pyridoxal kinase inhibitors, In Silico Pharmacol., 11 6. https://doi.org/10.1007/s40203-023-00142-8.

Ugbe, F.A., Shallangwa, G.A., Uzairu, A., Abdulkadir, I., 2023a. In-silico design and evaluation of the anti-wolbachia potential of boron-pleuromutilins, Borneo J. Pharm., 6 (2) 168–181. https://doi.org/10.33084/bjop.v6i2.4677.

Ugbe, F.A., Shallangwa, G.A., Uzairu, A., Abdulkadir, I., 2023b. A 2-D QSAR modeling, molecular docking study and design of 2-arylbenzimidazole derivatives as novel leishmanial inhibitors: a molecular dynamics study, Adv. J. Chem. Sect. A., 6 (1) 50–64. https://doi.org/10.22034/AJCA.2023.365873.1337.

Ugbe, F.A, Shallangwa, G.A, Uzairu, A., Abdulkadir, I., 2021. Activity modeling, molecular docking and pharmacokinetic studies of some boron-pleuromutilins as anti-wolbachia agents with potential for treatment of filarial diseases, Chem. Data Collect., 36 100783. https://doi.org/10.1016/j.cdc.2021.100783.

Ugbe, F.A., Shallangwa, G.A, Uzairu, A., Abdulkadir, I., 2022b. A combined 2-D and 3-D QSAR modeling, molecular docking study, design, and pharmacokinetic profiling of some arylimidamide-azole hybrids as superior L. donovani inhibitors, Bull. Natl. Res. Cent., 46 189. https://doi.org/10.1186/s42269-022-00874-1.

Ugbe, F.A., Shallangwa, G.A., Uzairu, A., Abdulkadir, I., Edache, E.I, Al-Megrin, W.A., Al-Shouli, S.T., Wang, Y., 2023c. Cheminformatics-based discovery of new organoselenium compounds with potential for the treatment of cutaneous and visceral leishmaniasis, Journal of Biomolecular Structure and Dynamics, 13830-13853. https://doi.org/10.1080/07391102.2023.2279269.

Velcicky J, Mathison C.J.N, Nikulin V, Pflieger D, Epple R, Azimioara M, Cow C, Michellys P.Y, Rigollier P, Beisner D.R, Bodendorf U, Guerini D, Liu B, Wen B, Zaharevitz S, Brandl T., 2019. Discovery of Orally Active Hydroxyethylamine-Based SPPL2a Inhibitors. ACS Med Chem Lett., 10 (6):887-892. https://doi.org/10.1021/acsmedchemlett.

Vinay K., Achintya S., Kunal R., 2023. Multi-target QSAR modeling for the identification of novel inhibitors against Alzheimer's disease, Chemometrics and Intelligent Laboratory Systems, 233, 104734, ISSN 0169-7439, https://doi.org/10.1016/j.chemolab.2022.104734.

Yap C.W., 2011. PaDEL-descriptor: an open source software to calculate molecular descriptors and fingerprints. J Comput Chem., 32 (7):1466–1474.

List of Figures

Figure 1. Experimental versus predicted pIC_{50} values for the hydroxyethylamine derivatives using the GA-MLR QSAR model

Figure 2. Experimental pIC_{50} values versus residuals for the hydroxyethylamine derivatives predicted by the GA-MLR model

Figure 3. Williams plot (standardized residuals vs leverage) for the QSAR model compounds

Figure 4. Y-scrambling plot showing the distribution of R^2 and Q^2 values for randomized models compared with the original QSAR model

Figure 5. Protein–ligand interactions of (a) donepezil, the reference drug, and (b) ligand 10 with the BACE1 inhibitor (PDB ID: 2ZHV).

Figure 6. Protein–ligand interactions of (a) donepezil, the reference drug, and (b) ligand 10 with the AChE inhibitor (PDB ID: 4EYZ).

Figure 7. Protein–ligand interactions of (a) donepezil, the reference drug, and (b) ligand 10 with the D2 Dopamine receptor (PDB ID: 6CM4).

Figure 8. Protein–ligand interactions of (a) donepezil, the reference drug, and (b) ligand 10 with the FGFR3 receptor (PDB ID: 6LVM).

Figure 9. Oral bioavailability radars of compounds B2 and B5.

Figure 10. Docked poses of designed ligand B2 with (A) BACE1 (PDB ID: 2ZHV), (B) AChE (PDB ID: 4EYZ), (C) D2 Dopamine receptor (PDB ID: 6CM4), and (D) FGFR3 (PDB ID: 6LVM).

Figure 11. Docked poses of designed ligand B5 with (A) BACE1 (PDB ID: 2ZHV), (B) AChE (PDB ID: 4EYZ), (C) D2 Dopamine receptor (PDB ID: 6CM4), and (D) FGFR3 (PDB ID: 6LVM).

Figure 12. Molecular dynamics (MD) simulation results for 200 ns trajectories of the Alzheimer's inhibitor complexes: (A) RMSD, (B) RoG, (C) RMSF, (D) SASA, and (E) number of hydrogen bonds.

Supplementary Files

This is a list of supplementary files associated with this preprint. Click to download.

- Supplementaryinformation.docx